

Conservation-informed Graph Learning for Spatiotemporal Dynamics Prediction

Yuan Mi
Renmin University of China
Beijing, China
miyuan@ruc.edu.cn

Pu Ren
Northeastern University
Boston, Massachusetts, USA
ren.pu@northeastern.edu

Hongteng Xu
Renmin University of China
Beijing, China
hongtengxu@ruc.edu.cn

Hongsheng Liu
Huawei Technologies
Shenzhen, China
liuhongsheng4@huawei.com

Zidong Wang
Huawei Technologies
Shenzhen, China
wang1@huawei.com

Yike Guo
HKUST
Hong Kong, China
yikeguo@ust.hk

Ji-Rong Wen
Renmin University of China
Beijing, China
jrwen@ruc.edu.cn

Hao Sun*
Renmin University of China
Beijing, China
haosun@ruc.edu.cn

Yang Liu*
University of Chinese Academy of
Sciences
Beijing, China
liuyang22@ucas.ac.cn

Abstract

Data-centric methods have shown great potential in understanding and predicting spatiotemporal dynamics, enabling better design and control of the object system. However, pure deep learning models often lack interpretability, fail to obey intrinsic physics, and struggle to cope with the various domains. While geometry-based methods, e.g., graph neural networks (GNNs), have been proposed to further tackle these challenges, they still need to find the implicit physical laws from large datasets and rely excessively on rich labeled data. In this paper, we herein introduce the conservation-informed GNN (CiGNN), an end-to-end explainable learning framework, to learn spatiotemporal dynamics based on limited training data. The network is designed to conform to the general conservation law via symmetry, where conservative and non-conservative information passes over a multiscale space enhanced by a latent temporal marching strategy. The efficacy of our model has been verified in various spatiotemporal systems based on synthetic and real-world datasets, showing superiority over baseline models. Results demonstrate that CiGNN exhibits remarkable accuracy and generalization ability, and is readily applicable to learning for prediction of various spatiotemporal dynamics in a spatial domain with complex geometry.

*Corresponding authors.

Permission to make digital or hard copies of all or part of this work for personal or classroom use is granted without fee provided that copies are not made or distributed for profit or commercial advantage and that copies bear this notice and the full citation on the first page. Copyrights for components of this work owned by others than the author(s) must be honored. Abstracting with credit is permitted. To copy otherwise, or republish, to post on servers or to redistribute to lists, requires prior specific permission and/or a fee. Request permissions from permissions@acm.org.

KDD '25, August 3–7, 2025, Toronto, ON, Canada.

© 2025 Copyright held by the owner/author(s). Publication rights licensed to ACM.

ACM ISBN 979-8-4007-1245-6/25/08

<https://doi.org/10.1145/XXXXXX.XXXXXX>

CCS Concepts

• **Computing methodologies** → **Modeling and simulation**; **Neural networks**; • **Applied computing** → *Physics*.

Keywords

Graph learning, spatiotemporal dynamics prediction, conservation law

ACM Reference Format:

Yuan Mi, Pu Ren, Hongteng Xu, Hongsheng Liu, Zidong Wang, Yike Guo, Ji-Rong Wen, Hao Sun, and Yang Liu*. 2025. Conservation-informed Graph Learning for Spatiotemporal Dynamics Prediction. In *Proceedings of the 31st ACM SIGKDD Conference on Knowledge Discovery and Data Mining V.1 (KDD '25), August 3–7, 2025, Toronto, ON, Canada*. ACM, New York, NY, USA, 23 pages. <https://doi.org/10.1145/XXXXXX.XXXXXX>

1 Introduction

The principled and accurate modeling and simulation of spatiotemporal dynamical systems play an important role in many science and engineering applications, e.g., physics, meteorology, ecology, social science, material science, etc. Classical approaches are primarily rooted in the use of well-posed physics-based models, governed by a system of partial differential equations (PDEs) under certain initial conditions (ICs) and boundary conditions (BCs), where the solutions could be achieved by a properly chosen numerical solver [3]. Nevertheless, the complexity of real-world problems poses grand challenges that traditional physics-based techniques struggle to address, especially when the *prior* knowledge of physics is incomplete or repeated forward analyses are required to assimilate data.

The ever-growing availability of data opens up a new avenue to tackle these challenges, resulting in data-centric methods leveraging the power of machine learning. Tremendous efforts have been recently placed on developing statistical or deep learning approaches for modeling [10, 32, 40], predicting [6, 49, 50, 65], discovering [11, 16, 55], and controlling [5, 64] the complex behavior

of nonlinear dynamics. Moreover, graph neural networks (GNNs) [63, 66], which integrate topological structures with an inherent connection to the physical world, are uniquely positioned to address above issues. Above all methods learn representations from, but highly rely on, rich labeled datasets, which are often expensive to acquire from experiments or simulations in most scientific and engineering problems. Due to the model’s over-parameterized black-box nature, issues arise in the context of explainability, overfitting, and generalizability. Embedding the *prior* knowledge to form physics-informed learning has shown the potential to alleviate these fundamental issues [30], producing more robust models for reliable prediction [2].

To this end, we propose an end-to-end explainable learning framework, aka conservation-informed GNN (CiGNN), to learn complex spatiotemporal dynamics based on limited training data. The network is designed to conform to the general differential form of conservation law with a source term for spatiotemporal dynamics, essentially acting as a *prior* knowledge-based inductive bias to the learning process. Due to the existence of source terms (e.g., internal reaction, damping, external input), the system might be subjected to entropy inequality leading to a non-conservative state. Inspired by Noether’s theorem, we depict the conservation property and entropy inequality via the fundamental principle of symmetry [54], and then propose a symmetry-preserved MPNN (SymMPNN) module for feature representation learning which accounts for symmetric and asymmetric information passing in graph edges. The learning process is resorted to a multi-mesh graph which enables the network to capture local and non-local spatial dependency, facilitating the acquisition of more detailed information across scales. To improve the stability and accuracy of long-term rollout prediction, we design a latent time integrator in the network as a time marching strategy which models the temporal dependency between sequenced latent embeddings extracted from each SymMPNN layer. The efficacy of CiGNN has been demonstrated on both synthetic and real-world observed datasets for modeling various types of spatiotemporal dynamics within different domain geometric configurations. The primary contributions can be summarized as follows:

- We design a novel model to preserve the general conservation law based on the fundamental principle of symmetry.
- Our proposed spatial and temporal schemes effectively control the error accumulation for long-term prediction.
- The CiGNN exhibits remarkable accuracy with limited training data (e.g., a few or dozens of datasets), and possesses generalization capability (over ICs, BCs and geometry meshes) in learning complex spatiotemporal dynamics, showing superiority over several representative baselines.

2 Related Works

Over the past few decades, classical numerical methods [14, 27] were dominated in the forward and inverse physics problems. However, the development of this field reaches a bottleneck until the emergence of deep learning methods, which changes the status quo.

Physics-informed learning. As one of the most popular framework, the seminal development of the physics-informed neural network (PINN) [29, 45] has enabled learning in small data regimes

for forward and inverse analyses of PDEs, where the loss function is regularized by the PDE residual. Such a differentiable paradigm has kindled enthusiastic attention in the past few years, which, together with its variant schemes, has been demonstrated effective in modeling and discovering a wide range of complex systems including fluid flows [46], subsurface transport [23], cardiovascular systems [4], deformation of solid continua [39], material constitutive relations [52], governing equation discovery [12], among many others. However, PINN generally has the need of explicit governing equations and the issue of scalability, resorting to the use of fully-connected neural networks and mesh-free point-wise training.

Neural operators. Another framework, neural operator, is designed to learn the underlying Green’s functions of PDEs, offering an alternative to model spatiotemporal dynamics, which possess generalizability and do not require *a priori* knowledge of the explicit PDE formulation [61, 62]. Neural operators, including DeepONet [37], Fourier neural operator (FNO) [35], and their variant algorithms [34, 57], have taken remarkable leaps in approximating the solution of PDE systems. However, the generalizability of these models largely depends on the richness of the labeled training data. When the complexity of the considered system remains high (e.g., multi-dimensional spatiotemporal dynamics in an irregular domain geometry), these methods might suffer from scalability issues with deteriorated performance.

Geometric learning. Recently, geometric learning of system dynamics has drawn great attention [22, 43, 58], where graphs, regardless of Euclidean or non-Euclidean meshes, are employed to represent physical features and provide naturally structured relationships (e.g., spatial proximity) with interpretability [9, 36, 60]. For example, message-passing neural networks (MPNNs) have been regarded as an effective form of graph neural network (GNN) in simulating dynamics of particle assembly [53], continuum media [42] and rigid bodies [21], as well as forecasting global weather [33]. In particular, when the explicit PDE formulation is completely unknown or partially missing, a recent study [25] shows that forcibly encoding the law of thermodynamics into the GNN architecture can boost the generalizability of the model for simulation of quasi-static deformable bodies. Moreover, the model in [19] is designed to deal with lattice meshes and the graph solver in [28] is rooted in the assumption of conservative systems to update the discretized conservation equation in the latent space via hard encoding.

3 Preliminary and Problem Statement

Learning to predict the dynamics of complex spatiotemporal systems based on limited training data (e.g., sparsely, and perhaps non-uniformly, sampled in space and time) is regarded as a great challenge [7]. Our objective is to tackle this challenge via creating a new explainable and generalizable learning framework adaptable to a broad category of spatiotemporal dynamics. Drawing from the fundamental insights of physics, we recognize the existence of numerous conservation laws within the physical realm. In general, the strong form of these conservation laws necessitates that, in order for a conserved quantity at a specific point to alter, there must exist a flow or flux of that quantity either into or out of that point. For example, the conservation law with a source term for

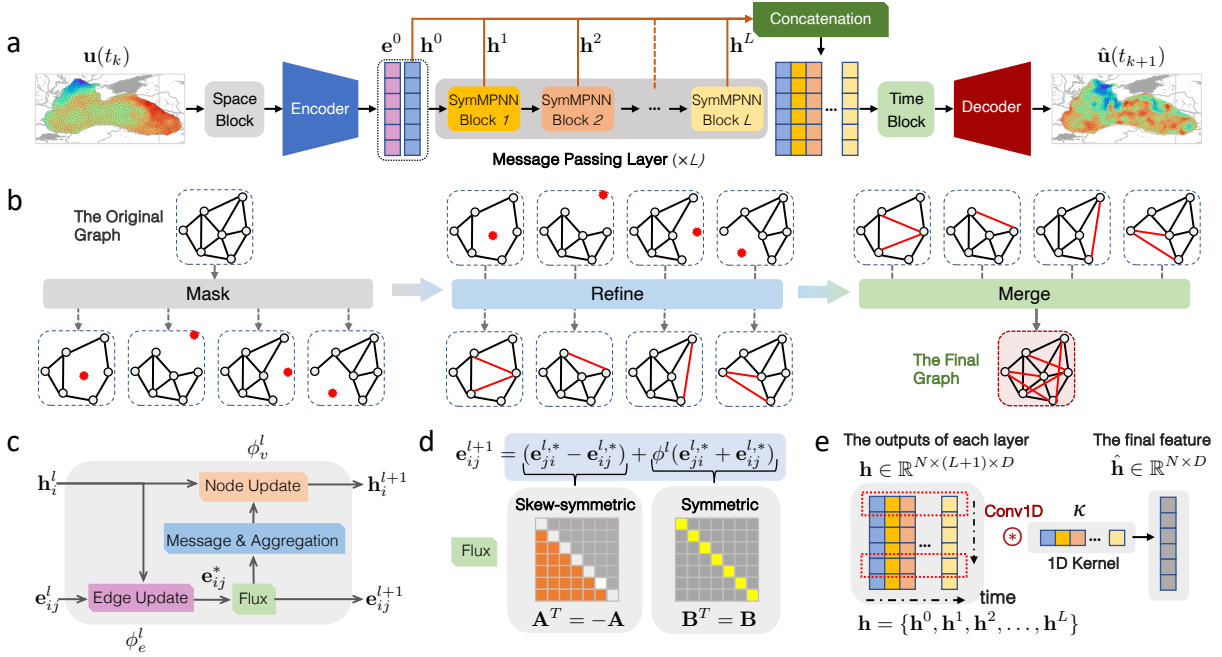


Figure 1: Schematic of the CiGNN model. a, The main network architecture. b, The space block that defines a multi-mesh graph to account for different scales and transforms the physical system state to a low-dimensional graph representation. c, The SymMPNN block that is designed for learning high-dimensional graph representation. d, The Flux update component that passes symmetric and asymmetric information in graph edges. e, The time block that marches the sequenced high-dimensional features.

spatiotemporal dynamics can be presented through a continuity equation, given by

$$\frac{\partial \mathbf{u}}{\partial t} + \nabla \cdot \mathcal{F}(\mathbf{u}) = \mathbf{s}(\mathbf{u}; \mathbf{x}, t) \quad (1)$$

where $\mathbf{u}(\mathbf{x}, t) \in \mathbb{R}^d$ denotes the system state variable vector composed of d components, $\mathbf{x} \in \mathbb{R}^m$ the m -dimensional spatial coordinate, t the time, ∇ the Nabla operator, $\mathcal{F}(\cdot) \in \mathbb{R}^{m \times d}$ the flux function, and $\mathbf{s}(\cdot) \in \mathbb{R}^d$ the source term. This equation models the evolution of the system state $\mathbf{u}(\mathbf{x}, t)$ over time as the composition of local flux term and the source term.

Now we consider an unstructured mesh of a m -dimensional domain (regardless of regular or irregular geometry), where the system state measured at a generic discrete time step t_k ($k = 1, 2, \dots, T'$) is denoted by $\mathbf{u}(t_k) \in \mathbb{R}^{N \times d}$. Here, N represents the number of graph nodes (observation grid points) and T' the number of time steps. Our aim is to establish a model to learn spatiotemporal dynamics on a predefined graph $G = (V, E, w)$, which underlines the intrinsic mapping between the input state variable $\mathbf{u}(t_k)$ and the output subsequent s time series $\{\hat{\mathbf{u}}(t_{k+1}), \dots, \hat{\mathbf{u}}(t_{k+s})\}$. Here, V is a set of nodes, E a set of edges connecting the nodes V , and $w(\cdot, \cdot) : E \rightarrow \mathbb{R}^1$ the edge weight function. For simplicity, $w(\mathbf{u}_i, \mathbf{u}_j)$ is expressed by w_{ij} and $w(\mathbf{u}_j, \mathbf{u}_i)$ by w_{ji} . In the same way, this simplicity also applies to the edge update function $F(\cdot, \cdot)$.

Conservation on graph. Given on the theory of graph calculus, the general conservation law in Eq. 1 can be reformulated into a discrete form on graph (see Appendix Subsection B.2 for detailed

derivation), shown as follows.

$$\frac{\partial \mathbf{u}_i}{\partial t} = \frac{1}{2} \sum_{j \in \mathcal{N}_i} (\sqrt{w_{ji}} F_{ji} - \sqrt{w_{ij}} F_{ij}) + \mathbf{s}(\mathbf{u}_i). \quad (2)$$

We realize that the conservation term can be formulated by the skew-symmetric tensor and the inequality by the symmetric tensor [56]. Instead of constructing such tensors directly, we implicitly build a learnable scheme to retain the above structure property, namely,

$$\frac{\partial \mathbf{u}_i}{\partial t} = \sum_{j \in \mathcal{N}_i} \left(\underbrace{F_{ji} - F_{ij}}_{\text{skew-symmetric}} + \underbrace{\phi(F_{ji} + F_{ij})}_{\text{symmetric}} \right), \quad (3)$$

where $\phi(\cdot)$ is a differential function to model the inequality and, meanwhile, learn the unknown source term (e.g., entropy inequality). Here, the skew-symmetric and symmetric features on the right-hand side of Eq. 3 are constructed to approximate the conservation and inequality principles, respectively. Meanwhile, we omit the coefficient of 1/2 for convenience.

4 Methodology

We develop a learning scheme that conforms to the conservation law shown in Eq. 1. More details are described in Appendix Section B. We will release the source code and data at <https://www.github.com> after peer review.

4.1 Conservation-informed graph neural network

The CiGNN architecture is composed of five key blocks, as shown in Figure 1a, including the space block, the encoder, the SymMPNN block, the time block, and the decoder. Here, the encoder lifts the low-dimensional quantities to a high-dimensional representation, and in the meantime the decoder projects the updated high-dimensional latent features to the evolved physical state. The space block (see Figure 1b) defines a multi-mesh graph to account for different scales and transforms the physical system state to a low-dimensional graph representation (e.g., node features, graph topology). Given the fact that the disturbance of existing source, such as internal reaction, damping or external input, breaks down the conservation, the system will be subjected to entropy inequality. We introduce a multi-layer SymMPNN module (see Figure 1c–d) as the core component for high-dimensional feature representation learning, where we construct symmetric and asymmetric matrices to pass non-conservative information in graph edges. In the next work, instead of treating the SymMPNN module as a step-by-step learning and acquisition of higher-order information in space, we view the multi-layer message-passing mechanism of SymMPNN as a process of cascaded transmission over time. This implies that implicit latent time intervals, either fixed or non-fixed, can be generated between the SymMPNN layers. Hence, we propose a simple but effective latent time integrator (see the time block depicted in Figure 1e) to march the sequenced high-dimensional features, which improves the stability and accuracy of long-range multi-step rollout prediction. Moreover, we provide a pseudo-code describing our proposed graph operator, as shown in Algorithm 1. More details of design motivation are shown in Appendix Subsection B.3.

4.2 Network architecture

4.2.1 Encoder. The Encoder lifts the physical state into latent features represented in a high-dimensional space. The encoded initial node features $\mathbf{h}_i^0 \in \mathbb{R}^c$ imply the physical state \mathbf{u}_i at the i th node, the corresponding position feature \mathbf{x}_i and the node type, where c denotes the channel size (aka, the dimension of the latent space). The encoded initial edge features $\mathbf{e}_{ij}^0 \in \mathbb{R}^c$ capture the relative positional information between the connected i th and j th nodes. Additionally, a variety of variables, such as angles, are encoded to enhance the expressiveness of the edge feature representation. The corresponding formulations are given by

$$\mathbf{h}_i^0 = \phi_v^{en}(\mathbf{u}_i \parallel \mathbf{x}_i \parallel \varkappa_i \parallel \dots), \quad (4a)$$

$$\mathbf{e}_{ij}^0 = \phi_e^{en}(\mathbf{x}_j - \mathbf{x}_i \parallel d_{ij} \parallel \vartheta_{ij}^x \parallel \vartheta_{ij}^y \parallel \dots), \quad (4b)$$

where $\phi_v^{en}(\cdot)$ and $\phi_e^{en}(\cdot)$ represent the learnable functions (e.g., MLPs); $\mathbf{x}_j - \mathbf{x}_i$ a vector that reflects the relative information between the i th and j th nodes; d_{ij} the relative distance in the physical space; \varkappa_i the i th node type; and $\vartheta_{ij}^x, \vartheta_{ij}^y$ the angle information of edge in different directions. In addition, $(\cdot \parallel \cdot)$ denotes the concatenation.

4.2.2 Processor. The Processor employs a graph with exclusively inter-node connections, where spatial and channel information from the local neighborhood of each node is aggregated through connections to adjacent nodes [53]. As shown in Figure 1a, it iteratively processes the high-dimensional latent features using a

Algorithm 1: Conservation-informed Graph Operator

Input: The current states $\mathbf{g}^l, \mathbf{h}_i^l, \mathbf{e}_{ij}^l$.

Output: The next states $\mathbf{g}^{l+1}, \mathbf{h}_i^{l+1}, \mathbf{e}_{ij}^{l+1}$.

while stop condition is not reached **do**

for each edge \mathbf{e}_{ij}^l **do**

 Gather sender and receiver nodes $\mathbf{h}_i^l, \mathbf{h}_j^l$;

 Compute output edge $\mathbf{e}_{ij}^{l*} = \phi_e^l(\mathbf{g}^l, \mathbf{h}_i^l, \mathbf{h}_j^l, \mathbf{e}_{ij}^l)$;

end

for each edge \mathbf{e}_{ij}^{l*} **do**

 Obtain the reversed edge \mathbf{e}_{ji}^{l*} with the edge \mathbf{e}_{ij}^{l*} ;

 Get the new edge state \mathbf{e}_{ij}^{l+1} with the flux function:

$$\mathbf{e}_{ij}^{l+1} = (\mathbf{e}_{ji}^{l*} - \mathbf{e}_{ij}^{l*}) + \phi^l(\mathbf{e}_{ij}^{l*} + \mathbf{e}_{ji}^{l*});$$

end

for each node \mathbf{h}_i^l **do**

 Aggregate \mathbf{e}_{ij}^{l+1} of per receiver, get the sum of the

$$\text{edge features } \tilde{\mathbf{e}}_i^{l+1} = \sum_{j \in \mathcal{N}_i} \mathbf{e}_{ij}^{l+1};$$

 Compute the new node-wise feature

$$\mathbf{h}_i^{l+1} = \phi_v^l(\mathbf{g}^l, \mathbf{h}_i^l, \tilde{\mathbf{e}}_i^{l+1});$$

end

 Aggregate all edges and nodes $\tilde{\mathbf{e}}^{l+1} = \sum_i^N \tilde{\mathbf{e}}_i^{l+1}$,

$$\tilde{\mathbf{h}}^{l+1} = \sum_i^N \mathbf{h}_i^{l+1};$$

 Compute new global features $\mathbf{g}^{l+1} = f_g(\mathbf{g}^l, \tilde{\mathbf{h}}^{l+1}, \tilde{\mathbf{e}}^{l+1})$;

end

return the next states $\mathbf{g}^{l+1}, \mathbf{h}_i^{l+1}, \mathbf{e}_{ij}^{l+1}$.

sequence of SymMPNN layers. For each layer, each node exchanges information with itself and its neighbors. Furthermore, the architecture incorporates residual connections between each processing layer, which allow for direct message passing at different scales. This part introduces the core component of the architecture, the conservation-informed graph operator (see Algorithm 1). The design of information passing across nodes and edges is inspired by the conservation on graph as shown in Eq. 3. Given a graph with available node and edge features, the mathematical formulation for the message-passing mechanism at each SymMPNN layer is defined as

$$\mathbf{e}_{ij}^{l*} = \phi_e^l(\mathbf{h}_i^l \parallel \mathbf{h}_j^l \parallel \mathbf{e}_{ij}^l), \quad (5a)$$

$$\mathbf{e}_{ij}^{l+1} = \underbrace{(\mathbf{e}_{ji}^{l*} - \mathbf{w}^l \circ \mathbf{e}_{ij}^{l*})}_{\text{asymmetric}} + \underbrace{\phi^l(\mathbf{e}_{ij}^{l*} + \mathbf{e}_{ji}^{l*})}_{\text{symmetric}}, \quad (5b)$$

$$\mathbf{h}_i^{l+1} = \phi_v^l\left(\mathbf{h}_i^l \parallel \sum_{j \in \mathcal{N}_i} \mathbf{e}_{ij}^{l+1}\right), \quad (5c)$$

where $\mathbf{h}_i^l \in \mathbb{R}^c$ and $\mathbf{h}_j^l \in \mathbb{R}^c$ denote the high-dimensional node features at nodes i and j , respectively, at the l th SymMPNN layer;

$\mathbf{e}_{ij}^l \in \mathbb{R}^c$ the high-dimensional edge features between the i th and j th nodes; $\mathbf{e}_{ij}^{l,*} \in \mathbb{R}^c$ and $\mathbf{e}_{ji}^{l,*} \in \mathbb{R}^c$ the corresponding intermediate edge features (e.g., bidirectional) inferred to represent symmetric and asymmetric information passing; $\phi_e^l(\cdot)$ the edge update function (e.g., MLP); $\mathbf{w}^l \in \mathbb{R}^c$ the trainable weights shared over the entire graph for the l th layer; \mathcal{N}_i the neighborhood node's index set for node i ; and \circ the Hadamard product. Here, \mathbf{e}_{ij}^{l+1} facilitates the learning process by strictly obeying the conservation law and the inequality principle. $\phi_v^l(\cdot)$ is a node update function (e.g., MLP) and $\phi^l(\cdot)$ a flux update function (e.g., MLP) for symmetric message passing.

We found that, when $\mathbf{w}^l \equiv 1$, the proposed CiGNN model achieves a more reliable performance. For comparison purpose, we remove the symmetric update part as shown in Eq. 5b while only keeping the asymmetric portion. Thus, we obtain two variant models, namely, CiGNN⁻ ($\mathbf{w}^l \equiv 1$) and CiGNN* ($\mathbf{w}^l \neq 1$, which is trainable).

4.2.3 Decoder. The Decoder maps updated high-dimensional latent features back to the original physical domain, which receives input from the Processor and generates the predicted increment for the last time step as output. This increment is then added as residue to the initial state to determine the new state. The learning process at the Decoder is given by

$$\hat{\mathbf{u}}_i(t + \Delta t) = \phi_v^{de}(\mathbf{h}_i^L) + \mathbf{u}_i(t), \quad (6)$$

where $\phi_v^{de}(\cdot)$ is a differentiable function (e.g., MLP) and L the total number of SymMPNN layers.

4.3 Spatial and temporal learning strategies

4.3.1 Space Block with multi-mesh strategy. Consider a graph with $G = (V, E)$, where V denotes the node set and E the edge set. The multi-mesh strategy involves three steps: (1) defining G^k as the initial graph; (2) randomly discarding a proportion of nodes in G^k to generate a new graph G^{k+1} as the subsequent initial graph; (3) iteratively repeating the second step, and aggregating all graphs into G . We organize the generated graphs by layers, designating the graph with the most node count as the topmost layer and the one with the fewest nodes as the bottom layer. In other words, as k increases ($k = 0, 1, 2, \dots$), the resulting graph structure G^{k+1} contains fewer nodes. Then, we define a refinement ratio $r \in [0, 1]$ to characterize the relationship between node numbers in the context graph. For instance, if G^k has N nodes, then the subsequent graph, G^{k+1} , will have rN nodes. We specifically set the refinement ratio r to 0.1 in this study. Experimental results concerning the selection of r are discussed in Appendix Table S7. The overall graph G can be conceptualized as the union of all edges and nodes:

$$G = \bigcup_k G^k, \quad G^k = (V^k, E^k), \quad k = 0, \dots, m. \quad (7)$$

Noting that the nodes in G^{k+1} are always the node subset of G^k , and the edge reconstruction process can capture information across extended distances. This leads to a multi-scale mesh distribution, enabling the network to capture both local and non-local relationships and learn complex detailed information. Meanwhile, the

multi-mesh technique performs edge reconstruction only during pre-processing (e.g., not training), following the random masking of nodes at each level. As shown in Figure 1b, the mask operation generates numerous subgraphs, which can alleviate the over-reliance on local information and enhance node-level feature extraction. Generally, the multi-mesh strategy can facilitate acquiring the key structural information.

4.3.2 Time Block with trainable temporal integration. We treat the multi-layer message-passing mechanism of SymMPNN as a process of cascaded transmission over time. A series of fixed or non-fixed sub-time intervals Δt_j^* are generated implicitly, e.g., $\Delta t_j^* \in [0, \Delta t_k]$, where $j = 0, 2, \dots, L-1$ and Δt_k denotes the physical time step. Given this assumption, each SymMPNN layer can be regarded as the evolution of information over one time interval. This is equivalent to the sub-stepping process commonly used in numerical integration methods. Additionally, a Taylor series expansion shows that the method is consistent if and only if the sum of the coefficients α_j is equal to one, described as

$$\mathbf{h}^L = \mathbf{h}^0 + \sum_{j=0}^{L-1} \alpha_j \mathbf{K}_j \quad \text{s.t.} \quad \sum_{j=0}^{L-1} \alpha_j = 1, \quad (8a)$$

$$\mathbf{K}_{j+1} = \varphi_{j+1} \left(t + \Delta t_j^*, \mathbf{h}^0 + \beta_j \mathbf{K}_j \right), \quad (8b)$$

where α_j, β_j are scalar, $\mathbf{K}_0 = \mathbf{h}^0$ the initial node features, φ_{j+1} the learnable function in the $(j+1)$ th SymMPNN block, and L the total number of SymMPNN layers.

Notably, this temporal integration strategy is realized on the high-dimensional space, so the coefficients α_j, β_j are also learnable latent features. \mathbf{K}_L denotes the output of final SymMPNN layer, which is the L -order approximation of solution. Each increment in our method can be viewed as the product of the coefficients β_j and an estimated slope specified by each function φ_j . The total increment is the sum of the weighted increments. To this end, we employ a trainable 1D convolutional filter to approximate the coefficients in Eqs. 8a and 8b, as shown in Figure 1d. This temporal integration strategy does not lead to extra cost for network training and inference.

5 Experiments

5.1 Datasets and Baselines.

To verify the efficacy of CiGNN for learning complex spatiotemporal dynamics on graphs, we consider four different systems shown in Appendix Table S2, e.g., the 2D Burgers equation, a 3D Gray-Scott (GS) reaction-diffusion (RD) system, the 2D incompressible flow past a cylinder (CF), and the Black Sea (BS) hydrological observation (see Figure 2). The datasets of the first three systems were spatiotemporally down-sampled (e.g., 5-fold in time) from high-fidelity data generated by direct numerical simulations considering different ICs, BCs, and meshes, while the last one was compiled from field measurements. Additional information, including data generation statistics and example trajectories, can be found in Appendix Table S3. We selected four baseline models for comparison (see Appendix Subsection C.3 for more details), including deep operator network (DeepONet) [38], Fourier neural operator (FNO) [35], mesh-based graph network (MGN) [42], and message-passing

Table 1: Summary of each model’s performance in terms of prediction error, e.g., aggregated root mean square error (RMSE) between the predicted and ground truth test data. Here, “–” denotes the model is unable or unsuitable to learn the dynamics (e.g., inapplicable to handle irregular mesh). “MP-PDE*” means that no gradient is backward propagated except for the last step. The bold values and underlined values represent the optimal and sub-optimal results on various datasets. “Pro.” means the promotion value which is calculated from the optimal and sub-optimal results. The one-step prediction results are shown in Appendix Table S9.

Model	2D Burgers ($\Delta t = 0.001$ s)	3D GS RD ($\Delta t = 0.001$ s)	2D CF ($\Delta t = 0.01$ s)	2D BS ($\Delta t = 1$ day)
DeepONet	3.7752×10^{-1}	1.3954×10^1	9.1095×10^{-1}	2.8696×10^0
FNO	1.6005×10^{-2}	1.5184×10^{-1}	–	–
MGN	1.8955×10^{-2}	1.0350×10^{-2}	<u>1.5790×10^{-1}</u>	<u>6.9512×10^{-1}</u>
MP-PDE*	1.6280×10^{-2}	<u>1.0186×10^{-2}</u>	2.4511×10^{-1}	9.0051×10^{-1}
MP-PDE	<u>1.5551×10^{-2}</u>	1.0843×10^{-2}	1.6412×10^{-1}	6.9621×10^{-1}
CiGNN	4.2916×10^{-3}	8.3840×10^{-3}	1.2561×10^{-1}	6.5503×10^{-1}
Pro. (%) \uparrow	72.4	17.7	20.4	5.7

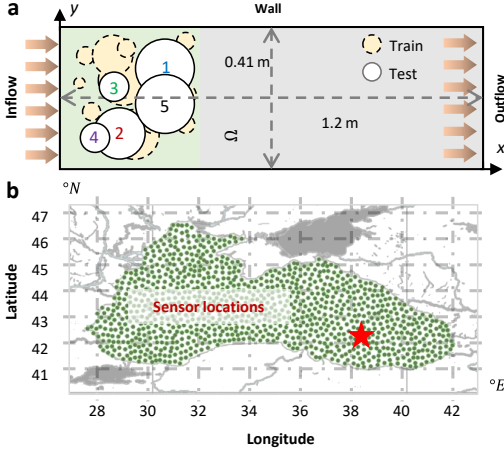


Figure 2: Diagrams of irregular domains. a, Schematic diagram of the CF example setup with the fluid flowing in from the left (inflow) to the right (outflow). b, The geographic and sensor information of the BS Real-world dataset.

PDE solver (MP-PDE) [8], with hyperparameters listed in Appendix Tables S11–S13.

5.2 Loss function

The training procedure is to minimize the discrepancy between the labeled and the predicted data. The loss function of our model is defined as

$$\mathcal{L}(\theta) = \frac{1}{dSN\tilde{T}} \sum_{\alpha=1}^S \left\| \text{vec}(\hat{U}^{(\alpha)}) - \text{vec}(U^{(\alpha)}) \right\|_2^2, \quad (9)$$

which calculates the aggregated mean square errors (MSE) between the rollout-predicted data $\hat{U}^{(\alpha)} \in \mathbb{R}^{N \times d \times \tilde{T}}$ and the training labels $U^{(\alpha)} \in \mathbb{R}^{N \times d \times \tilde{T}}$ to optimize the trainable parameters (θ) in our model. Here, $\text{vec}(\cdot)$ denotes the vectorization operation; d the system dimension; N the total number of mesh grid points; \tilde{T} the

number of rollout time steps in training; and S the total number of grouped training samples.

5.3 Evaluation metrics

The root mean squared error (RMSE) and the Pearson correlation coefficient (PCC) are utilized as the evaluation metrics, given by

$$RMSE(\mathbf{U}, \hat{\mathbf{U}}) = \sqrt{\frac{1}{dNT} \left\| \text{vec}(\hat{\mathbf{U}}) - \text{vec}(\mathbf{U}) \right\|_2^2}, \quad (10a)$$

$$PCCs(\mathbf{U}, \hat{\mathbf{U}}) = \frac{\text{cov}[\text{vec}(\hat{\mathbf{U}}), \text{vec}(\mathbf{U})]}{\sigma_{\mathbf{u}} \sigma_{\hat{\mathbf{u}}}}, \quad (10b)$$

where $\hat{\mathbf{U}} \in \mathbb{R}^{N \times d \times T}$ and $\mathbf{U} \in \mathbb{R}^{N \times d \times T}$ denote the predicted and true system states, respectively; $\text{cov}[\cdot, \cdot]$ the covariance function; $\sigma_{\mathbf{u}}$ and $\sigma_{\hat{\mathbf{u}}}$ the standard deviations of \mathbf{U} and $\hat{\mathbf{U}}$, respectively; and T the total number of considered time steps. In addition, introducing noise to the training data can stabilize the model and improve the generalization ability for learning spatiotemporal dynamics [42, 53]. Therefore, we add a small amount of Gaussian noise in the training data to improve the CiGNN’s performance.

5.4 Training settings and computational resources

For a fair comparison, we train each model ten times and select the one with the median performance according to the evaluation of the validation datasets. We train all models for 1,000 epochs and set early stopping with a patience of 100 epochs. We utilize the GELU activation function [41] for all MLP hidden layers, while linear activation is considered for the output layers. Additionally, layer normalization is applied after each MLP to improve the training convergence, except for those in the Decoder. All models are trained using the Adam Optimizer [31] and the ReduceLROnPlateau learning scheduler [41] which decays the learning rate by a factor of 0.8. The encoder module consists of a 2-layer MLP with a hidden size of 128, and the decoder has a 2-layer MLP with a hidden size of 128. We only use 4 SymMPNN blocks for the processor, where 2 layer

MLPs with a hidden size of 128 are employed as the node, edge and flux update functions. The same hyperparameters are used in MGN, MP-PDE, and CiGNN. Notably, all the hyperparameters are selected from various ranges. For example, the learning rate is selected from the set $[10^{-1}, 10^{-2}, 10^{-3}, 10^{-4}, 10^{-5}]$. More details about the hyperparameter test are given in Appendix Tables S4 to S8. The models were trained on the NVIDIA A100 GPU (80GB) on an Intel(R) Xeon(R) Platinum 8380 CPU (2.30GHz, 64 cores) server. More details are given in Appendix Section D.

5.5 Results

5.5.1 2D Convection-Diffusion system. The results listed in Table 1 show that CiGNN consistently outperforms other baseline models in the context of prediction accuracy. Figure 3a displays the distribution of prediction errors as well as the predicted snapshots at a typical time step (0.995 s) by different methods. The CiGNN model lifts the prediction accuracy by 1~2 orders of magnitude in terms of MSE metric compared with all other baselines. Due to the meshless and point-wise nature of DeepONet, it falls short in scalable modeling of higher dimensional spatiotemporal dynamics. Given the squared domain with structured grid mesh, FNO produces a moderate prediction result in the situation with limited training data. The performance of MP-PDE aligns with that of MGN. Note that MP-PDE is a derivative of MGN with the primary distinction in their decoder components, e.g., MGN employs multilayer perceptron (MLP) while MP-PDE utilizes convolution for decoding. Despite discrepant performance of other models, CiGNN generalizes well to ICs and maintains a high prediction accuracy, which demonstrates notable strength and shows clear superiority over the baselines.

5.5.2 3D Reaction-Diffusion system. The results reported in Table 1 once again show our CiGNN model achieves the best performance. Figure 3b displays the prediction error distribution and typical snapshots for the GS RD system at 713.75 s. Similar to the previous example, FNO, renowned for its potency in the realm of operator learning, appears to inadequately grasp the underlying dynamics of the GS RD equation in the regime of small training data. Unfortunately, DeepONet exhibits little progress in learning the intricate evolution of the 3D system states, e.g., the prediction over time still deviates clearly from actual values yielding large errors. The results serve to substantiate that both MGN and MP-PDE, based on the multi-step rollout training strategy, maintain robustness. However, CiGNN still outperforms other models, showing its superior potential in learning spatiotemporal dynamics in a 3D space.

5.5.3 2D Flow past a cylinder. Our model CiGNN generalizes well over Re and BCs as well as graph meshes in the CF example, which again outperforms the baselines as depicted in Table 1. Figure 3c displays the snapshots of the predicted flow field at time 8.55 s in the generalization test, where the cylinder size and position as well as the domain mesh remain different from those in the training datasets. Notably, generalizing the learning model on various CF datasets poses grand challenges due to the varying mesh node counts and graph structures, exacerbated by the introduction of random cylinder positions that lead to variant Reynolds numbers. Since FNO struggles with irregular mesh structures, we opted not

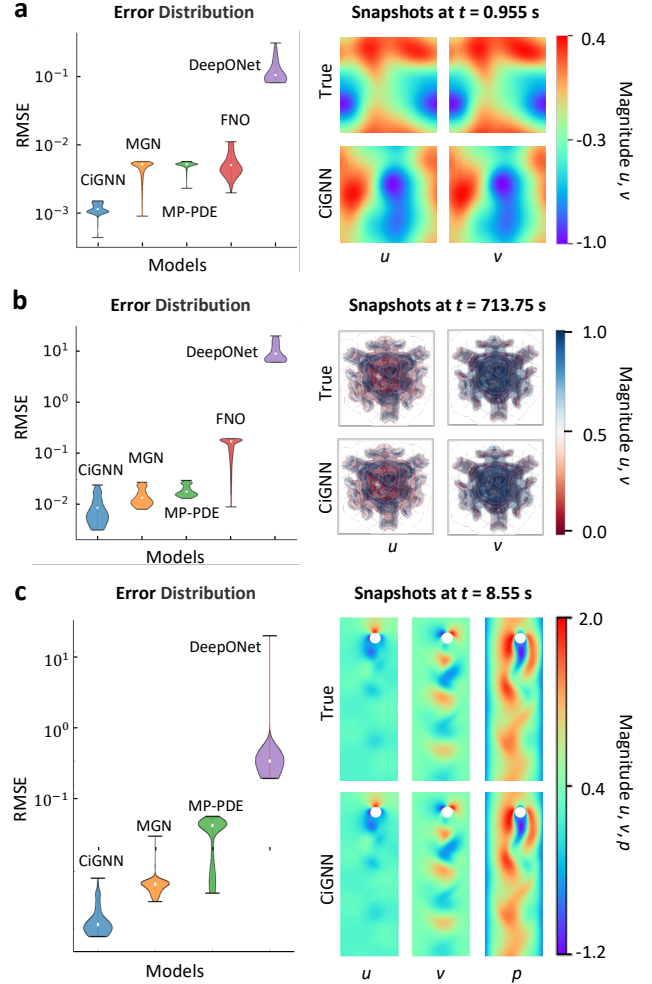


Figure 3: Error distributions and the system state snapshots predicted by CiGNN and other baselines. More results are shown in Appendix Figures S2–S3. a, The 2D viscous Burgers equation example. b, The 3D Gray-Scott equation example. c, Schematic diagram of the CF example setup with the fluid flowing in from the left (inflow) to the right (outflow).

to include it in the comparison experiments. The point-wise meshless learning scheme of DeepONet might suffer from the scalability issue, which, as a result, leads to failure in the CF example. The distribution of performance for MGN remains a similar trend illustrated previously. However, MP-PDE shows deterioration compared to the previous two examples. Overall, CiGNN surpasses other baseline models in various degrees. Figure 3c shows two additional generalization test results concerning varying domain meshes as well as different locations and sizes (e.g., from small to large) of the cylinder. It can be seen from Figure 3c that as the cylinder size decreases, Re increases and the flow becomes more turbulent. Nevertheless, CiGNN can still accurately predict the turbulent flow dynamics.

Table 2: Ablation results on four datasets. Here, the symbol “-” represents that Task #2 on CF dataset does not exist since multi-mesh strategy is not utilized. The bold values and underlined values represent the optimal and sub-optimal results on various datasets.

Task	Method	2D Burgers ($\Delta t = 0.001s$)	3D GS RD ($\Delta t = 0.001s$)	2D CF ($\Delta t = 0.01s$)	2D BS ($\Delta t = 1day$)
#1	w/o flux update	1.0012×10^{-2}	1.3138×10^{-2}	1.4526×10^{-1}	6.9581×10^{-1}
#2	w/o multi-mesh	9.8175×10^{-3}	1.1101×10^{-2}	-	6.9456×10^{-1}
#3	w/o temporal	<u>9.2089×10^{-3}</u>	<u>9.5921×10^{-3}</u>	<u>1.2740×10^{-1}</u>	<u>6.5589×10^{-1}</u>
#0	CiGNN (Full)	4.2916×10^{-3}	8.3840×10^{-3}	1.2561×10^{-1}	6.5503×10^{-1}

5.5.4 2D Hydrological dynamics forecast of the Black Sea. We employ the trained CiGNN model to conduct a 20-day-long forecasting of the hydrological dynamics of the Black Sea. Figure 4a–b show the results of the predicted water flow velocities and sea surface temperature. It is evident that our model effectively captures the evolution patterns of the hydrological dynamics, especially for low-frequency information that dominates the overall trend (as can be seen from the predicted snapshots). The correlation values for both the velocity and temperature fields consistently lie above 0.8, indicating an accurate prediction even in the presence of unknown uncertainties. The correlation curve in Figure 4c–d illustrates that the prediction of the temperature exhibits relatively scattered with a larger deviation. This might be because the temperature data, captured at a depth of 12 meters below sea level, remains less susceptible to the influence of other external factors. Yet, this real-world dataset considered in this example encompasses numerous elusive variables that are absent from our model’s training data which consists solely of velocity and temperature variables. Consequently, this limitation hampers accurate predictions of localized high-frequency information, deteriorating the performance of CiGNN. Commonly, this issue can be ameliorated by augmenting the training data with pertinent variables to enhance the model’s predictive capability.

5.6 Ablation study

To gain deeper insights into how each component of the model affects its overall performance, we conducted an ablation study based on the aforementioned datasets. The results show that the removal of each module leads to deteriorated performance of the model as shown in Table 2. We summarize the observations as follows:

- Results in Task #1 demonstrate that, while the promotion may vary, both the conservative and inequality principles play significant roles across different datasets.
- Results in Task #2 indicate that a larger number of edges in the global context leads to more accurate prediction. Our proposed trade-off strategy of constructing sparse graphs at different scales greatly improves performance.
- Results in Task #3 show that our temporal learning strategy effectively mitigates error propagation issues with a high-order scheme. In particular, we observe that the performance of the temporal strategy is sensitive to the size of the single-step time interval.

Table 3: Results of ablation tests on the temporal integration strategy for the 2D Burgers dataset. Here, TCN stands for the temporal convolutional network and LSTM denotes the long short-term memory network. Each model was trained for 1000 iterations with one-step strategy. The integration strategies are denoted by “P1” (our proposed 1D convolution filter), “P2” (2D convolution filter), “P3” (TCN with 1D convolution filter), and “P4” (LSTM).

Case	No. of layers	Temporal strategy	No. of parameters	RMSE
C1	4	None	514,950	9.5812×10^{-2}
C2	16	None	1,901,958	1.7593×10^{-1}
C3	4	P1 (ours)	515,007	6.9040×10^{-2}
C4	16	P1 (ours)	1,902,567	1.2442×10^{-1}
C5	4	P2	514,993	8.3591×10^{-2}
C6	16	P2	1,902,001	1.6049×10^{-1}
C7	4	P3	514,968	8.7441×10^{-2}
C8	16	P3	1,902,012	1.6872×10^{-1}
C9	4	P4	779,142	1.2820×10^{-1}
C10	16	P4	2,166,150	2.2104×10^{-1}

We also consider two variants of CiGNN, namely, CiGNN⁻ and CiGNN*, where only the asymmetric information passing is considered in the SymMPNN blocks. As depicted in Appendix Table S10, the result shows the efficacy of the symmetric information-passing component. In the case of BS dataset, CiGNN* outperforms CiGNN, which indicates that the effective learning of the inequality term in real-world scenarios is not fully guaranteed.

Moreover, we provide the ablation results on comparison of various temporal integration strategies shown in Table 3. It is evident that a 4-layer CiGNN model with the simplest 1D convolution filter-based strategy (denoted by C3, with minimal parameter overhead) achieves the best performance, surpassing other strategies including the 2D convolution filtering, TCN and LSTM, demonstrating that our temporal strategy (1D Conv filter) plays a key role in CiGNN to improve the model’s long-term rollout prediction accuracy. More detailed discussion can be found in Appendix Subsection E.3.

6 Conclusion

This paper introduces an end-to-end graph-based deep learning model (namely, CiGNN) to predict the evolution of complex spatiotemporal dynamics. The CiGNN model is designed to preserve

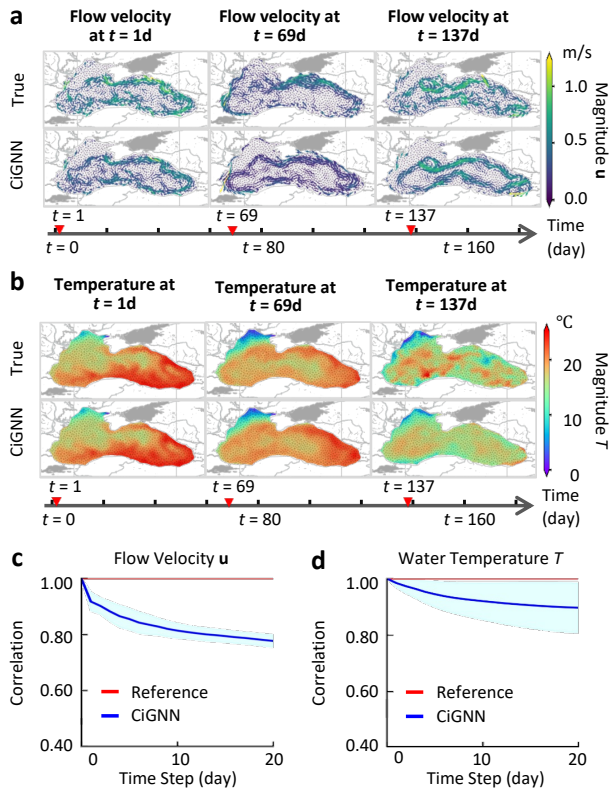


Figure 4: Prediction results of CiGNN on real-world BS hydrological dataset. a–b, Snapshots of the predicted flow velocity and water temperature at day 1, day 69, and day 137. c–d, Pearson correlation of the corresponding predicted flow velocity and water temperature. The above three time points represent the sampling moments during the early, middle, and late stages of prediction, respectively. The blue line represents the mean value of the correlation, and the light blue area the deviation (e.g., $\pm\sigma$).

the general differential form of conservation law with a source term based on the fundamental principle of symmetry. To this end, we devise a novel SymMPNN module, equipped with symmetric asymmetric information passing in graph edges, for graph representation learning. The embedding of such *a priori* knowledge into the network architecture design amounts to adding an inductive bias to the learning process, relaxing the need for heavy training data. Moreover, the performance of CiGNN is further lifted by a multi-mesh spatial strategy and a latent temporal integrator. The resulting graph learning model is explainable and, meanwhile, the trained model generalizes to predict complex spatiotemporal dynamics over varying ICs, BCs and geometry meshes. The efficacy of the CiGNN model was evaluated in forecasting the dynamics of a variety of spatiotemporal systems (e.g., convection-diffusion system, reaction-diffusion system, flow past a cylinder, and the hydrological dynamics of the Black Sea) based on both synthetic and field-observed datasets. Given limited training data, we demonstrated that the CiGNN model identifies well the underlying dynamics and shows remarkable accuracy.

Despite its demonstrated efficacy and potential, CiGNN is faced with two main challenges that need to be addressed in the future. On one hand, the brute-force implementation of CiGNN might suffer from the computational bottleneck (e.g., the multi-step rollout training requires heavy memory overhead that depends linearly on the number of rollout steps), which would result in a scalability issue. On the other hand, the present model is only deployed to model a classical fluid dynamics problem (e.g., flow past a cylinder), whereas its capacity for predicting highly complex turbulent flows (e.g., large Re , complex BCs that induce wall effect, etc.) remains unknown. We aim to systematically tackle these challenges in our future study.

Acknowledgments

The work is supported by the National Natural Science Foundation of China (No. 62276269, No. 92270118), the Beijing Natural Science Foundation (No. 1232009), the Strategic Priority Research Program of the Chinese Academy of Sciences (No. XDB0620103), and the National Key R&D Program of China (No. 2021ZD0110400). H. Sun would like to thank the support from the Fundamental Research Funds for the Central Universities and the Research Funds of Renmin University of China (No. 202230265). Y. Liu would like to thank the support from the Fundamental Research Funds for the Central Universities (No. E2EG2202X2). P. Ren would like to disclose that he was involved in this work when he was at Northeastern University, who has not been supported by Huawei Technologies.

References

- [1] Abien Fred Agarap. 2018. Deep learning using rectified linear units (relu). *arXiv preprint arXiv:1803.08375* (2018).
- [2] Alex Alberts and Ilias Biliotis. 2023. Physics-informed information field theory for modeling physical systems with uncertainty quantification. *J. Comput. Phys.* 486 (2023), 112100.
- [3] William F Ames. 2014. *Numerical methods for partial differential equations*. Academic Press, Inc.
- [4] Amirhossein Arzani, Jian-Xun Wang, and Roshan M D’Souza. 2021. Uncovering near-wall blood flow from sparse data with physics-informed neural networks. *Physics of Fluids* 33, 7 (2021).
- [5] Giacomo Baggio, Danielle S Bassett, and Fabio Pasqualetti. 2021. Data-driven control of complex networks. *Nature Communications* 12, 1 (2021), 1429.
- [6] Kaifeng Bi, Lingxi Xie, Hengheng Zhang, Xin Chen, Xiaotao Gu, and Qi Tian. 2023. Accurate medium-range global weather forecasting with 3D neural networks. *Nature* 619, 7970 (2023), 533–538.
- [7] Nicolas Boullé, Diana Halikias, and Alex Townsend. 2023. Elliptic PDE learning is provably data-efficient. *Proceedings of the National Academy of Sciences* 120, 39 (2023), e2303904120.
- [8] Johannes Brandstetter, Daniel Worrall, and Max Welling. 2022. Message passing neural PDE solvers. In *International Conference on Learning Representations*.
- [9] Michael M Bronstein, Joan Bruna, Taco Cohen, and Petar Veličković. 2021. Geometric deep learning: Grids, groups, graphs, geodesics, and gauges. *arXiv preprint arXiv:2104.13478* (2021).
- [10] Steven L Brunton, Bernd R Noack, and Petros Koumoutsakos. 2020. Machine learning for fluid mechanics. *Annual Review of Fluid Mechanics* 52 (2020), 477–508.
- [11] Steven L Brunton, Joshua L Proctor, and J Nathan Kutz. 2016. Discovering governing equations from data by sparse identification of nonlinear dynamical systems. *Proceedings of the National Academy of Sciences* 113, 15 (2016), 3932–3937.
- [12] Zhao Chen, Yang Liu, and Hao Sun. 2021. Physics-informed learning of governing equations from scarce data. *Nature Communications* 12, 1 (2021), 6136.
- [13] Djork-Arné Clevert, Thomas Unterthiner, and Sepp Hochreiter. 2015. Fast and accurate deep network learning by exponential linear units (elus). *arXiv preprint arXiv:1511.07289* (2015).
- [14] Robert Eymard, Thierry Gallouët, and Raphaële Herbin. 2000. Finite volume methods. *Handbook of numerical analysis* 7 (2000), 713–1018.
- [15] R. Farina, S. Dobricic, A. Storto, S. Masina, and S. Cuomo. 2015. A revised scheme to compute horizontal covariances in an oceanographic 3D-VAR assimilation

- system. *J. Comput. Phys.* 284 (2015), 631–647. <https://doi.org/10.1016/j.jcp.2015.01.003>
- [16] Daniel Floryan and Michael D Graham. 2022. Data-driven discovery of intrinsic dynamics. *Nature Machine Intelligence* 4, 12 (2022), 1113–1120.
- [17] Justin Gilmer, Samuel S Schoenholz, Patrick F Riley, Oriol Vinyals, and George E Dahl. 2017. Neural message passing for quantum chemistry. In *International conference on machine learning*. PMLR, 1263–1272.
- [18] Xavier Glorot and Yoshua Bengio. 2010. Understanding the difficulty of training deep feedforward neural networks. In *Proceedings of the Thirteenth International Conference on Artificial Intelligence and Statistics*, Vol. 9. 249–256.
- [19] Ivan Grega, Ilyes Batatia, Gábor Csányi, Sri Karlapati, and Vikram S Deshpande. 2024. Energy-conserving equivariant GNN for elasticity of lattice architected metamaterials. *arXiv preprint arXiv:2401.16914* (2024).
- [20] Will Hamilton, Zhitao Ying, and Jure Leskovec. 2017. Inductive representation learning on large graphs. *Advances in Neural Information Processing Systems* 30 (2017).
- [21] Jiaqi Han, Wenbing Huang, Hengbo Ma, Jiachen Li, Josh Tenenbaum, and Chuang Gan. 2022. Learning physical dynamics with subequivariant graph neural networks. *Advances in Neural Information Processing Systems* 35 (2022), 26256–26268.
- [22] Zhongkai Hao, Zhengyi Wang, Hang Su, Chengyang Ying, Yinpeng Dong, Songming Liu, Ze Cheng, Jian Song, and Jun Zhu. 2023. Gnot: A general neural operator transformer for operator learning. In *International Conference on Machine Learning*. PMLR, 12556–12569.
- [23] QiZhi He and Alexandre M Tartakovsky. 2021. Physics-Informed Neural Network Method for Forward and Backward Advection-Dispersion Equations. *Water Resources Research* 57, 7 (2021), e2020WR029479.
- [24] Dan Hendrycks and Kevin Gimpel. 2016. Gaussian error linear units (gelus). *arXiv preprint arXiv:1606.08415* (2016).
- [25] Quercus Hernández, Alberto Badiás, Francisco Chinesta, and Elías Cueto. 2023. Thermodynamics-informed neural networks for physically realistic mixed reality. *Computer Methods in Applied Mechanics and Engineering* 407 (2023), 115912. <https://doi.org/10.1016/j.cma.2023.115912>
- [26] Hans Hersbach, Bill Bell, Paul Berrisford, Shoji Hirahara, András Horányi, Joaquín Muñoz-Sabater, Julien Nicolas, Carole Peubey, Raluca Radu, Dinand Schepers, et al. 2020. The ERA5 global reanalysis. *Quarterly Journal of the Royal Meteorological Society* 146, 730 (2020), 1999–2049.
- [27] Anil Nirmal Hirani. 2003. *Discrete exterior calculus*. California Institute of Technology.
- [28] Masanobu Horie and Naoto Mitsume. 2024. Graph Neural PDE Solvers with Conservation and Similarity-Equivariance. *arXiv preprint arXiv:2405.16183* (2024).
- [29] Ameya D Jagtap, Ehsan Kharazmi, and George Em Karniadakis. 2020. Conservative physics-informed neural networks on discrete domains for conservation laws: Applications to forward and inverse problems. *Computer Methods in Applied Mechanics and Engineering* 365 (2020), 113028.
- [30] George Em Karniadakis, Ioannis G Kevrekidis, Lu Lu, Paris Perdikaris, Sifan Wang, and Liu Yang. 2021. Physics-informed machine learning. *Nature Reviews Physics* 3, 6 (2021), 422–440.
- [31] Diederik P. Kingma and Jimmy Ba. 2015. Adam: A Method for Stochastic Optimization. In *International Conference on Learning Representations*.
- [32] Dmitrii Kochkov, Jamie A Smith, Ayva Alieva, Qing Wang, Michael P Brenner, and Stephan Hoyer. 2021. Machine learning-accelerated computational fluid dynamics. *Proceedings of the National Academy of Sciences* 118, 21 (2021), e2101784118.
- [33] Remi Lam, Alvaro Sanchez-Gonzalez, Matthew Willson, Peter Wirnsberger, Meire Fortunato, Ferran Alet, Suman Ravuri, Timo Ewalds, Zach Eaton-Rosen, Weihua Hu, et al. 2023. Learning skillful medium-range global weather forecasting. *Science* 382, 6677 (2023), 1416–1421.
- [34] Samuel Lanthaler, Roberto Molinaro, Patrik Hadorn, and Siddhartha Mishra. 2023. Nonlinear Reconstruction for Operator Learning of PDEs with Discontinuities. In *International Conference on Learning Representations*.
- [35] Z. Li, N. B. Kovachki, K. Azizzadenesheli, B. Liu, K. Bhattacharya, A. Stuart, and A. Anandkumar. 2021. Fourier Neural Operator for Parametric Partial Differential Equations. In *International Conference on Learning Representations*.
- [36] Yang Liu, Jiashun Cheng, Haihong Zhao, Tingyang Xu, Peilin Zhao, Fugee Tsung, Jia Li, and Yu Rong. 2024. SEGNO: Generalizing Equivariant Graph Neural Networks with Physical Inductive Biases. In *The Twelfth International Conference on Learning Representations*.
- [37] Lu Lu, Pengzhan Jin, Guofei Pang, Zhongqiang Zhang, and George Em Karniadakis. 2021. Learning nonlinear operators via DeepONet based on the universal approximation theorem of operators. *Nature Machine Intelligence* 3, 3 (2021), 218–229.
- [38] Lu Lu, Pengzhan Jin, Guofei Pang, Zhongqiang Zhang, and George Em Karniadakis. 2021. Learning nonlinear operators via DeepONet based on the universal approximation theorem of operators. *Nature Machine Intelligence* 3, 3 (2021), 218–229. <https://doi.org/10.1038/s42256-021-00302-5>
- [39] Sijun Niu, Enrui Zhang, Yuri Bazilevs, and Vikas Srivastava. 2023. Modeling finite-strain plasticity using physics-informed neural network and assessment of the network performance. *Journal of the Mechanics and Physics of Solids* 172 (2023), 105177.
- [40] Shaowu Pan, Steven L Brunton, and J Nathan Kutz. 2023. Neural implicit flow: a mesh-agnostic dimensionality reduction paradigm of spatio-temporal data. *Journal of Machine Learning Research* 24, 41 (2023), 1–60.
- [41] Adam Paszke, Sam Gross, Francisco Massa, Adam Lerer, James Bradbury, Gregory Chanan, Trevor Killeen, Zeming Lin, Natalia Gimelshein, Luca Antiga, et al. 2019. Pytorch: An imperative style, high-performance deep learning library. *Advances in neural information processing systems* 32 (2019).
- [42] T. Pfaff, M. Fortunato, A. Sanchez-Gonzalez, and P. Battaglia. 2021. Learning Mesh-Based Simulation with Graph Networks. In *International Conference on Learning Representations*.
- [43] Jesús Pineda, Benjamin Midtvedt, Harshith Bachimanchi, Sergio Noé, Daniel Midtvedt, Giovanni Volpe, and Carlo Manzo. 2023. Geometric deep learning reveals the spatiotemporal features of microscopic motion. *Nature Machine Intelligence* 5, 1 (2023), 71–82.
- [44] Alyssa Quek, Zhiyong Wang, Jian Zhang, and Dagan Feng. 2011. Structural image classification with graph neural networks. In *International Conference on Digital Image Computing: Techniques and Applications*. 416–421.
- [45] Maziar Raissi, Paris Perdikaris, and George E Karniadakis. 2019. Physics-informed neural networks: A deep learning framework for solving forward and inverse problems involving nonlinear partial differential equations. *Journal of Computational physics* 378 (2019), 686–707.
- [46] Maziar Raissi, Alireza Yazdani, and George Em Karniadakis. 2020. Hidden fluid mechanics: Learning velocity and pressure fields from flow visualizations. *Science* 367, 6481 (2020), 1026–1030.
- [47] Prajit Ramachandran, Barret Zoph, and Quoc V Le. 2017. Searching for activation functions. *arXiv preprint arXiv:1710.05941* (2017).
- [48] Chengping Rao, Pu Ren, Qi Wang, Oral Buyukozturk, Hao Sun, and Yang Liu. 2023. Encoding physics to learn reaction-diffusion processes. *Nature Machine Intelligence* 5, 7 (2023), 765–779.
- [49] Suman Ravuri, Karel Lenc, Matthew Willson, Dmitry Kangin, Remi Lam, Piotr Mirowski, Megan Fitzsimons, Maria Athanassiadou, Sheleem Kashem, Sam Madge, et al. 2021. Skillful precipitation nowcasting using deep generative models of radar. *Nature* 597, 7878 (2021), 672–677.
- [50] Francesco Regazzoni, Luca Dede, and Alfio Quarteroni. 2019. Machine learning for fast and reliable solution of time-dependent differential equations. *Journal of Computational physics* 397 (2019), 108852.
- [51] Pu Ren, Chengping Rao, Yang Liu, Jian-Xun Wang, and Hao Sun. 2022. PhyCRNet: Physics-informed convolutional-recurrent network for solving spatiotemporal PDEs. *Computer Methods in Applied Mechanics and Engineering* 389 (2022), 114399.
- [52] Shahed Rezaei, Ahmad Moeineddin, and Ali Harandi. 2024. Learning solutions of thermodynamics-based nonlinear constitutive material models using physics-informed neural networks. *Computational Mechanics* (2024), 1–34.
- [53] Alvaro Sanchez-Gonzalez, Jonathan Godwin, Tobias Pfaff, Rex Ying, Jure Leskovec, and Peter Battaglia. 2020. Learning to simulate complex physics with graph networks. In *International Conference on Machine Learning*. 8459–8468.
- [54] Willy Sarlet and Frans Cantrijn. 1981. Generalizations of Noether’s theorem in classical mechanics. *Siam Review* 23, 4 (1981), 467–494.
- [55] Michael Schmidt and Hod Lipson. 2009. Distilling free-form natural laws from experimental data. *Science* 324, 5923 (2009), 81–85.
- [56] Eitan Tadmor. 1984. Skew-selfadjoint form for systems of conservation laws. *J. Math. Anal. Appl.* 103, 2 (1984), 428–442.
- [57] Alasdair Tran, Alexander Mathews, Lexing Xie, and Cheng Soon Ong. 2023. Factorized Fourier Neural Operators. In *International Conference on Learning Representations*.
- [58] Haixin Wang, Jiaxin Li, Anubhav Dwivedi, Kentaro Hara, and Tailin Wu. 2024. BENO: Boundary-embedded Neural Operators for Elliptic PDEs. *arXiv preprint arXiv:2401.09323* (2024).
- [59] Max Welling and Thomas N Kipf. 2016. Semi-supervised classification with graph convolutional networks. In *J. International Conference on Learning Representations (ICLR 2017)*.
- [60] Liming Wu, Zhichao Hou, Jirui Yuan, Yu Rong, and Wenbing Huang. 2024. Equivariant spatio-temporal attentive graph networks to simulate physical dynamics. *Advances in Neural Information Processing Systems* 36 (2024).
- [61] Tailin Wu, Takashi Maruyama, and Jure Leskovec. 2022. Learning to accelerate partial differential equations via latent global evolution. *Advances in Neural Information Processing Systems* 35 (2022), 2240–2253.
- [62] Tailin Wu, Willie Neiswanger, Hongtao Zheng, Stefano Ermon, and Jure Leskovec. 2024. Uncertainty Quantification for Forward and Inverse Problems of PDEs via Latent Global Evolution. In *Proceedings of the AAAI Conference on Artificial Intelligence*, Vol. 38. 320–328.
- [63] Zonghan Wu, Shirui Pan, Fengwen Chen, Guodong Long, Chengqi Zhang, and S Yu Philip. 2020. A comprehensive survey on graph neural networks. *IEEE transactions on neural networks and learning systems* 32, 1 (2020), 4–24.
- [64] Zheng-Meng Zhai, Mohammadamin Moradi, Ling-Wei Kong, Bryan Glaz, Mulugeta Haile, and Ying-Cheng Lai. 2023. Model-free tracking control of complex dynamical trajectories with machine learning. *Nature Communications* 14, 1

(2023), 5698.

[65] Yuchen Zhang, Mingsheng Long, Kaiyuan Chen, Lanxiang Xing, Ronghua Jin, Michael I Jordan, and Jianmin Wang. 2023. Skilful nowcasting of extreme precipitation with NowcastNet. *Nature* 619, 7970 (2023), 526–532.

[66] Ziwei Zhang, Peng Cui, and Wenwu Zhu. 2020. Deep learning on graphs: A survey. *IEEE Transactions on Knowledge and Data Engineering* 34, 1 (2020), 249–270.

A Background

The study of spatiotemporal dynamics aims to explore and elucidate the dynamic behavior, pattern formation, instability, and predictive capabilities of complex systems. Understanding spatiotemporal dynamics is crucial for addressing practical challenges in various domains, including physics, chemistry, engineering, climate science, etc. Recently, machine learning (ML) has shown great promise in modeling domain-specific scientific problem governed by partial differential equations (PDEs). In this paper, we focus on graph neural networks (GNNs) to learn spatiotemporal PDE systems.

A.1 Conventional GNNs

A classic GNN [59] is composed of three main components: an embedding layer for the input features, a stack of GNN layers, and a final task-based layer. In a graph $G = (V, E)$ where V contains $n = |V|$ nodes and E is the set of edges, the connectivity of the graph is represented by the adjacent matrix $\mathbf{A} \in \mathbb{R}^{n \times n}$. Here, $\mathbf{A}_{ij} = 1$ if there exists an edge between the nodes i and j , otherwise $\mathbf{A}_{ij} = 0$. The degree matrix is denoted as $\mathbf{D} \in \mathbb{R}^{n \times n}$.

A.2 Conventional MPNNs

For simplicity, we describe the process of message-passing neural networks (MPNNs) [17] on the undirected graph G with node features \mathbf{h}_i and edge features \mathbf{e}_{ij} . The forward pass has two phases, a message-passing phase and an update phase. The message-passing phase is expressed by message function ϕ_e and the update phase is described by vertex update function ϕ_v . The network layers are indexed by l and $\mathbf{h}^{l=0}$ denotes the node features of the initial input layer. During these two phase, the hidden state \mathbf{h}_i^{l+1} at node i in the graph are updated by the messages $\mathbf{e}_{ij}^{l,*}$ and its last hidden state \mathbf{h}_i^l according to

$$\mathbf{e}_{ij}^{l,*} = \phi_e^l(\mathbf{h}_i^l \parallel \mathbf{h}_j^l \parallel \mathbf{e}_{ij}^l), \quad (\text{S1a})$$

$$\mathbf{h}_i^{l+1} = \phi_v^l\left(\mathbf{h}_i^l \parallel \sum_{j \in \mathcal{N}_i} \mathbf{e}_{ij}^{l,*}\right), \quad (\text{S1b})$$

where in the l th layer, the edge feature between i th node and j th node is indicated by \mathbf{e}_{ij}^l . The edge feature \mathbf{e}_{ij}^{l+1} is updated along the message propagation ϕ_e^l . Here, the message function ϕ_e^l and vertex update function ϕ_v^l are both learnable differentiable functions (e.g., MLPs). The operation $(\cdot \parallel \cdot)$ denotes concatenation operation between the embedding features. The symbol \mathcal{N}_i in the function ϕ_v^l denotes the neighbor's index set of the i th node in graph G .

A.3 Variables Notation

Moreover, we present a summary of the variable notations used in our paper, as detailed in Table S1.

B Methodology

This section provides the supplementary information for the methodology described in the Main Text.

B.1 Preliminary of Graph Calculus

Let $G = (V, E)$ be a connected finite graph, which includes $|V|$ nodes and $|E|$ edges containing all edges between vertices in V . In the scalar or vector field, the sum of degrees is formulated as $\sum_{u_i \in V} \text{deg}(u_i) = 2|E|$, where the symbol $\text{deg}(u_i)$ denotes the number of edges that are incident to the vertex u_i . Under the aforementioned conditions, we furnish the relevant definitions below.

Definition 1: With a vertex function $f: V \rightarrow \mathbb{C}$, the symbol $\nabla_{ij} f$ for $j \in \mathcal{N}_i$ is described as follows:

$$\nabla_{ij} f = f(u_j) - f(u_i), \quad (\text{S2})$$

where \mathcal{N}_i denotes all other nodes within the neighborhood of node u_i and we simplify the subscript $u_i u_j$ as ij .

Definition 2: With a vertex function $f: V \rightarrow \mathbb{C}$, the symbol $\nabla_{ij} f^2$ for $j \in \mathcal{N}_i$ is defined as

$$\nabla_{ij} f^2 = f(u_j)^2 - f(u_i)^2. \quad (\text{S3})$$

Definition 3: With any vertex function $f: V \rightarrow \mathbb{C}$ and $g: V \rightarrow \mathbb{C}$, the symbol $\nabla_{ij}(fg)$ for $j \in \mathcal{N}_i$ is formulated as follows:

$$\begin{aligned} \nabla_{ij}(fg) &= f(u_j)g(u_j) - f(u_i)g(u_i) \\ &= f(u_j)(g(u_j) - g(u_i)) + (f(u_j) - f(u_i))g(u_i) \\ &= f(u_j)\nabla_{ij}(g) + \nabla_{ij}(f)g(u_i) \\ &= (\nabla_{ij}(f) + f(u_i))\nabla_{ij}(g) + \nabla_{ij}(f)g(u_i) \\ &= \nabla_{ij}(f)\nabla_{ij}(g) + f(u_i)\nabla_{ij}(g) + \nabla_{ij}(f)g(u_i). \end{aligned} \quad (\text{S4})$$

Definition 4: For $j \in \mathcal{N}_i$, the gradient of vertex function f at any $u_i \in V$ is given by

$$\nabla f(u_i) = (\nabla_{ij} f). \quad (\text{S5})$$

Definition 5: For $j \in \mathcal{N}_i$ on G , the scalar product of any vector field $\mathbf{W}(u_i) = (\bar{w}_{ij})$ and $\mathbf{U}(u_i) = (\bar{u}_{ij})$ is given by

$$\mathbf{W}(u_i) \cdot \mathbf{U}(u_i) = \sum_{j \in \mathcal{N}_i} \bar{w}_{ij} \bar{u}_{ij}. \quad (\text{S6})$$

Specifically, we have

$$|\mathbf{W}(u_i)|^2 = \sum_{j \in \mathcal{N}_i} \bar{w}_{ij}^2. \quad (\text{S7})$$

Definition 6: If f is a scalar function (i.e., a real-valued or complex-valued function) and $\mathbf{W}(u_i)$ is a vector field, their pointwise product can be written as follows:

$$(f\mathbf{W})(u_i) = f(u_i) \cdot \mathbf{W}(u_i), \quad (\text{S8})$$

where the function f scales each component of the vector field $\mathbf{W}(u_i)$ at every point u_i in space.

Definition 7: For $u_i \in V$, the directional derivative of function f along a vector field $\mathbf{W}(u_i)$ is defined by

$$\nabla_{\mathbf{W}f}(u_i) = \mathbf{W} \cdot \nabla f(u_i) = \sum_{j \in \mathcal{N}_i} \bar{w}_{ij} \nabla_{ij} f. \quad (\text{S9})$$

Then, the directional derivative of a function f along ∇f has the form of

$$\nabla_{\nabla f} f(u_i) = \sum_{j \in \mathcal{N}_i} \nabla_{ij} f \nabla_{ij} f = |\nabla f(u_i)|^2. \quad (\text{S10})$$

Table S1: Variables notation used in our paper.

Application Domain	Variable Description	Symbol	Role
2D Burgers Equation	x-component of velocity	$u(x, y, t)$	Input / Predicted
	y-component of velocity	$v(x, y, t)$	Input / Predicted
2D Navier-Stokes Equation	vorticity	$w(x, y, t)$	Input/Predicted
2D Gray-Scott Equation	concentrations of chemical species U	$u(x, y, t)$	Input/Predicted
	concentrations of chemical species V	$v(x, y, t)$	Input/Predicted
3D Gray-Scott Equation	concentrations of chemical species U	$u(x, y, z, t)$	Input/Predicted
	concentrations of chemical species V	$v(x, y, z, t)$	Input/Predicted
2D Cylinder Flow Dataset	x-component of velocity	$u(x, y, t)$	Input/Predicted
	y-component of velocity	$v(x, y, t)$	Input/Predicted
	pressure	$p(x, y, t)$	Input / Predicted
2D Black Sea Dataset	x-component of water flow velocity	$u(x, y, t)$	Input/Predicted
	y-component of water flow velocity	$v(x, y, t)$	Input/Predicted
	temperature in water depth of 12.5 meter	$T(x, y, t)$	Input/Predicted
Global Field	x-direction of space coordinate	x	Input
	y-direction of space coordinate	y	Input
	z-direction of space coordinate	z	Input
	time coordinate	t	Input
	time increment	Δt	Input
	space increment	$\Delta \mathbf{x}$	Input
	discrete timestamp at k th step	t_k	Input

Definition 8: For the vector field $\mathbf{W}(u_i)$ at $u_i \in V$, its divergence can be defined by

$$\text{div}(\mathbf{W}(u_i)) = \nabla \cdot \mathbf{W}(u_i) = \sum_{j \in \mathcal{N}_i} \bar{w}_{ij}. \quad (\text{S11})$$

Then, the divergence of $\nabla f(u_i)$ at $u_i \in V$, also named the laplacian operator, is given by

$$\text{div}(\nabla f(u_i)) = \sum_{j \in \mathcal{N}_i} \nabla_{ij} f = \nabla^2 f(u_i). \quad (\text{S12})$$

Divergence theorem: For $j \in \mathcal{N}_i, u_i \in V$, if $\bar{w}_{ij} = -\bar{w}_{ji}$, we have

$$\int_G \text{div}(\mathbf{W}(u_i)) = \sum_{u_i \in V} \sum_{j \in \mathcal{N}_i} \bar{w}_{ij} = 0. \quad (\text{S13})$$

PROOF. Set $\bar{w}_{ij} = 0$ for any $u_j \notin \mathcal{N}(u_i)$, then we have

$$\begin{aligned} \sum_{u_i \in V} \sum_{j \in \mathcal{N}_i} \bar{w}_{ij} &= \sum_{u_i \in V} \sum_{u_j \in V} \bar{w}_{ij} \\ &= \frac{1}{2} \sum_{u_i \in V} \sum_{u_j \in V} \bar{w}_{ij} + \frac{1}{2} \sum_{u_i \in V} \sum_{u_j \in V} \bar{w}_{ji} \\ &= 0. \end{aligned} \quad (\text{S14})$$

B.2 Conservative Property of CiGNN

Despite the complex behavior exhibited in spatiotemporal dynamic systems, conservation laws provide a means to simplify the analysis of these systems. For instance, in fluid dynamics, the conservation of mass (also named continuity equation) is the key to the

problem-solving. Our proposed graph approximator is inspired by this conservation principle linking the flux of a vector field through a closed surface to its divergence within the enclosed volume. Suppose volume \mathcal{V} is a compact subset of \mathbb{R}^3 and \mathcal{S} (also indicated with $\partial\mathcal{V}$) is its piecewise smooth boundary, we have the detailed description shown as follows.

Theorem 1: If there is a continuously differentiable tensor field \mathbf{F} on a neighborhood of \mathcal{V} , then we have that a volume integral over the volume \mathcal{V} is equal to the surface integral over the boundary of the volume \mathcal{V} :

$$\iiint_{\mathcal{V}} (\nabla \cdot \mathbf{F}) d\mathcal{V} = \iint_{\mathcal{S}} (\mathbf{F} \cdot \hat{\mathbf{n}}) d\mathcal{S}, \quad (\text{S15})$$

where $\hat{\mathbf{n}}$ is the outward-pointing unit normal. The conservation principle (e.g., the divergence-free condition) formulated in Theorem 1 implies that while the flow quantity within a local region changes over time, the global net flow in and out remains nearly constant. For further explanation, within the graph G , we denote $flow_{ij}$ as the flow that leaves from the node i , and $flow_{ji}$ the flow that enters to the node i . In a scalar or vector field, we consider that $flow_{ij} \geq 0$ and $flow_{ji} \leq 0$. Here, a key assumption underlying the physics law is that $flow_{ij} = -flow_{ji}$, for $(i, j) \in G$. Then, the conservation principle on the edge, or the divergence measurement on one vertex reads

$$flux_i = \sum_{(i, \cdot) \in G} flow_{i, \cdot} + \sum_{(\cdot, i) \in G} flow_{\cdot, i}, \quad (\text{S16})$$

where $flux_i$ denotes the total flow quantity through the i th node, and $flow_{i, \cdot}$ and $flow_{\cdot, i}$ the flows that leave and enter the node

i. Subsequently, an easy corollary of Theorem 1 is described as follows.

Corollary 1: *If the volume \mathcal{V} can be partitioned into some separate parts $\mathcal{V}_1, \mathcal{V}_2, \dots, \mathcal{V}_n$, the flux out $\Phi(\mathcal{V})$ of the original volume \mathcal{V} should be equal to the sum of flux through each component volume, namely,*

$$\Phi(\mathcal{V}) = \Phi(\mathcal{V}_1) + \Phi(\mathcal{V}_2) + \dots + \Phi(\mathcal{V}_n). \quad (\text{S17})$$

Given the above corollary, for a large domain, we can divide it into multiple subdomains for separate processing. Thus, we extend this theorem to the graph for learning spatiotemporal dynamics (e.g., PDEs) due to the essentially existence of subdomains of graph itself. Let $G = (V, E, w)$ be a undirected graph, where V is a set of nodes, E a set of edges connecting the nodes V , and $w : E \rightarrow \mathbb{R}^1$ the edge weight function. For simplicity, $w(u_i, u_j)$ is expressed by w_{ij} and $w(u_j, u_i)$ is expressed by w_{ji} .

Definition 1: *With a vertex function $f \in \mathcal{H}(V)$ along the edge $e_{ij} \in E$, the weighted graph derivative (or weighted difference) of u_i is expressed as:*

$$\partial_{u_i} f(u_i) := \sqrt{w_{ij}} (f(u_j) - f(u_i)), \quad (\text{S18})$$

where the edge weight function w_{ij} associates to every edge e_{ij} a value, namely, $w(u_i, u_j)$. Similarly, w_{ji} associates to every edge e_{ji} a value, namely, $w(u_j, u_i)$.

Definition 2: *Based on the weighted graph derivative, we define the linear weighted gradient operator on graphs $\nabla_w : \mathcal{H}(V) \rightarrow \mathcal{H}(E)$ as:*

$$(\nabla_w f)(u_i, u_j) = \partial_{u_i} f(u_i). \quad (\text{S19})$$

Definition 3: *The adjoint operator ∇_w^* of a edge function $F \in \mathcal{H}(E)$ at a vertex $u_i \in V$ has the following form:*

$$(\nabla_w^* F)(u_i) = \frac{1}{2} \sum_{j \in \mathcal{N}_i} \sqrt{w_{ij}} (F_{ji} - F_{ij}), \quad (\text{S20})$$

where \mathcal{N}_i denotes the neighborhood node's index set for node i . For simplicity, we simplified $F(u_i, u_j)$ as F_{ij} and $F(u_j, u_i)$ is simplified by F_{ji} .

Theorem 2: *For all $f \in \mathcal{H}(V), F \in \mathcal{H}(E)$, the linear adjoint operator $\nabla_w^* : \mathcal{H}(E) \rightarrow \mathcal{H}(V)$ of the weighted gradient operator should satisfy the following condition:*

$$\langle \nabla_w f, F \rangle_{\mathcal{H}(E)} = \langle f, \nabla_w^* F \rangle_{\mathcal{H}(V)}. \quad (\text{S21})$$

Definition 4: *Using the linear adjoint operator, the weighted divergence operator on graphs can be expressed as:*

$$\text{div}_w := -\nabla_w^*. \quad (\text{S22})$$

With above definition, we immediately get the following inference that the divergence on a graph can be interpreted as the *flux* of the edge function in each vertex of the graph. Then we rewrite the original PDE in Eq. 1 into the graph form as follows

$$\frac{\partial u_i}{\partial t} + \text{div}_w(F(u_i)) = s(u_i), \quad (\text{S23})$$

where $s(\cdot)$ represents the source term. Then, substituting Eqs. S20 and S22 into Eq. S23, we get the following equation:

$$\frac{\partial u_i}{\partial t} = \frac{1}{2} \sum_{j \in \mathcal{N}_i} \sqrt{w_{ij}} (F_{ji} - F_{ij}) + s(u_i). \quad (\text{S24})$$

It is noted that in a directed graph, w_{ij} may not be equal to w_{ji} , which aligns with the actual situation that there exist conservation and inequality terms which govern the dynamics. Hence, we rewrite Eq. S24 and obtain the following equation on a directed graph:

$$\frac{\partial u_i}{\partial t} = \frac{1}{2} \sum_{j \in \mathcal{N}_i} (\sqrt{w_{ji}} F_{ji} - \sqrt{w_{ij}} F_{ij}) + s(u_i). \quad (\text{S25})$$

We realize that the conservation term can be formulated by the skew-symmetric tensor and the inequality by the symmetric tensor [56]. Instead of constructing such tensors directly, we implicitly build a learnable scheme to retain the above structure property, namely,

$$\frac{\partial u_i}{\partial t} = \sum_{j \in \mathcal{N}_i} \left(\underbrace{F_{ji} - F_{ij}}_{\text{skew-symmetric}} + \phi \left(\underbrace{F_{ji} + F_{ij}}_{\text{symmetric}} \right) \right), \quad (\text{S26})$$

where $\phi(\cdot)$ is a differential function to model the inequality and, meanwhile, learn the unknown source term (e.g., entropy inequality). Here, we omit the coefficient of 1/2 for convenience. Here, the skew-symmetric and symmetric features on the right-hand side of Eq. S26 are constructed to approximate the conservation and inequality principles, respectively. In particular, we use the addition operation rather concatenation for the symmetric part in Eq. S26 to guarantee the invariance and interchangeability.

Note that the above derivation is done in the physical space, which inspires us to design a learnable model (e.g., CiGNN) in the latent space following a similar setting. The graph network is not restricted to highly regular structures, which, instead, can be applied to represent abstract relationships on any irregular meshes.

B.3 Spatial and Temporal Strategies

The motivations of our network design are two-fold in terms of feature extraction of spatial patterns and temporal evolution, respectively.

B.3.1 Spatial strategy. Firstly, GNNs have shown great potential for modeling spatiotemporal systems thanks to their inherent capacity to capture the dynamics in the physical world using graph structures. However, a critical observation reveals that current GNN models tend to overemphasize node features while neglecting the crucial aspect of edge features [20]. In particular, leveraging GNNs for modeling spatiotemporal dynamics should be able to include both explicit temporal changes in node states and implicit interactions via edges. The existing GNN models focus on processing edge features to align with data distribution without obeying *a priori* knowledge of physics principles. Hence, we introduce two forms of prior knowledge to ensure the GNN model conforming to the general conservation law, namely, symmetry (e.g., conservation) and asymmetry (e.g., entropy inequality), and design the SymMPNN block as a core graph learning module. These concepts draw inspiration from the well-known conservation law and principle of symmetry. Imposing hard constraints on GNN models via symmetry can facilitate the network convergence, enhance the model's interpretability, and improve the ability of spatial feature representation learning.

Table S2: Basic information of datasets.

Dataset	Domain	Physical parameters	No. of nodes	Trajectory length	Train/Validation/Test trajectories	Boundary condition	Force term
2D Burgers	Square $[0, 1]^2$	(u, v)	2,500 (50^2)	1,000	60 (50/5/5)	Periodic	No
3D GS RD	Cubic $[0, 96]^3$	(u, v)	13,824 (24^3)	3,000	10 (5/3/2)	Periodic	No
2D CF	Irregular	(u, v, p)	3,000~5,000	1,000	220 (200/10/10)	Unknown	No
2D BS	Irregular	(u, v, T)	1,000~40,000	365	29 (25/3/1)	Unknown	Unknown

B.3.2 Temporal strategy. Predicting the temporal evolution of dynamics can be cast as a Markov process. A simple approach to model such an evolution is resorted to numerical discretization and integration over time. Explicit time integration schemes are favorable and preferred in deep learning (e.g., MPNNs [42]) in the context of temporal forecasting (e.g., rollout prediction schemes), thanks to their straightforward implementation in a computational graph. However, if the time step between two evolved states is too big, it may cause instability issue. We are motivated to address this issue by proposing a learnable sub-stepping method. To this end, we view the message-passing process of the feedforward SymMPNN layers as the temporal propagation of dynamics at a finite number of sub-steps. Hence, we design a trainable temporal integrator to sequentially march the latent features of the SymMPNN layers so as to improve the model’s performance for long-range temporal prediction.

C Dataset and Baselines

We evaluate the performance of our proposed method and baseline models on three simulated datasets and one real-world weather data. For the generated datasets, we consider three different types of PDE systems, including 2D viscous Burgers equation, 3D Gray-Scott Reaction-Diffusion (GS RD) equation, and 2D unsteady incompressible Cylinder Flow (CF). Moreover, the real-world dataset is the atmospheric dynamics in the Black Sea (BS) field, where no explicit governing equations are considered. The detailed information of generating specific datasets can be found in Table S3. We compare our model with four representative baseline models, outlined as follows. And we make every effort to strike a balance between the model performance and the parameter count (e.g., typically aiming to keep it within the range of 500,000 to 600,000). The parameters of the relevant baseline models are shown from Table S11 to Table S13. Notably, all the hyperparameters are obtained from various ranges. For example, the learning rate is selected from the set $[10^{-1}, 10^{-2}, 10^{-3}, 10^{-4}, 10^{-5}]$.

C.1 Dataset Description

C.1.1 2D Burgers Equation. Convection-diffusion systems emerge from the interplay of the diffusion and convection (advection) processes, describing scenarios where particles, energy, or other physical attributes are transported in time and space. One of the most well-known PDEs used to model such phenomena is the viscous Burgers equation, commonly found in simplified fluid mechanics, nonlinear acoustics, and gas dynamics, expressed as (with the source term omitted) $\partial \mathbf{u} / \partial t = \mathbf{D} \nabla^2 \mathbf{u} - \mathbf{u} \cdot \nabla \mathbf{u}$. Here, $\mathbf{D} \in \mathbb{R}^{d \times d}$ denotes the diffusivity tensor, $\nabla^2 \mathbf{u}$ characterizes the diffusion, and

$\mathbf{u} \cdot \nabla \mathbf{u}$ represents the convection (or advection). In this example, we consider a 2D incompressible flow ($\mathbf{u} = [u, v]^T$) described by the Burgers equation, subjected to a randomized IC in a squared domain with periodic BCs.

C.1.2 3D Reaction-Diffusion system. The reaction-diffusion (RD) process is an interesting phenomenon commonly seen in nature, e.g., the interaction among chemical or biological substances, the formation of Turing patterns in the skin of tropical fishes, etc. Such a process emphasizes the role of intrinsic material diffusion and localized reactions in shaping system dynamics in space and time. Mathematically, it can be represented by the following PDE: $\partial \mathbf{u} / \partial t = \mathbf{D} \nabla^2 \mathbf{u} + \mathcal{R}(\mathbf{u})$, where $\mathbf{u} \in \mathbb{R}^d$ represents the concentration variables, $\mathbf{D} \in \mathbb{R}^{d \times d}$ the diffusion coefficient matrix, and $\mathcal{R}(\mathbf{u})$ the reaction term. Herein, we consider a GS RD equation in a 3D space (e.g., $\mathbf{x} \in \mathbb{R}^3$), which describes the reaction and diffusion of two chemical species ($\mathbf{u} = [u, v]^T$). The reaction equations for this system read $\mathcal{R}_u = -uv^2 + \alpha(1 - u)$ and $\mathcal{R}_v = uv^2 - (\alpha + \beta)v$, where α and β are the coefficients prescribing the reaction process.

C.1.3 2D Flow past a cylinder. We further consider a more challenging example (e.g., 2D fluid flow past a cylinder) to test the generalization ability of CiGNN over BCs. In practice, cylinder flow analysis is indispensable in scenarios such as fluid around bridge foundations, offshore drilling platform supports, underwater pipelines, and jetty piles. Here, the incompressible fluid flows into a channel ($1.2 \text{ m} \times 0.41 \text{ m}$) from left to right and passes a circular cylinder located near the left boundary, as depicted in Figure 3c. The flow dynamics can be modeled by the Navier-Stokes (NS) equation given by

$$\frac{\partial \mathbf{u}}{\partial t} + \nabla \cdot (\mathbf{u} \otimes \mathbf{u}) = \frac{1}{Re} \nabla^2 \mathbf{u} - \frac{1}{\rho} \nabla p, \quad (\text{S27a})$$

$$\nabla \cdot \mathbf{u} = 0, \quad (\text{S27b})$$

where $\mathbf{u} = [u, v]^T \in \mathbb{R}^2$ denotes the vector field of fluid velocity, ρ the fluid density, and \otimes the dyadic tensor product. Note that the pressure field $p \in \mathbb{R}^1$ constrains the flow and serves as a Lagrange multiplier to enforce the divergence-free condition of the fluid in Eq. S27b. The Reynolds number Re dictates the complexity of the fluid, e.g., turbulence occurs when $Re \gg 1$. For the particular example considered herein, the value of Re is inversely proportional to the cylinder size. We herein consider the location of the circular cylinder varies (resulting in the change of BCs) for the generation of different datasets (see Figure 3c), while the inflow velocity remains constant. Hence, Re is no longer a constant. As the fluid moves around the cylinder, the reduced cross-sectional area leads to accelerated velocity and decreased pressure along its path.

Table S3: Computational parameters for datasets generation. δx and δt denote the spatial and time spacing, respectively.

Dataset	PDE	Parameters	Size	$\delta t(s)$	δx
2D Burgers	Eq. S28	$\nu = 0.01, \lambda, \gamma \sim \mathcal{N}(0, 1), c \sim \mathcal{N}(-1, 1)$	$1,001 \times 2 \times 50^2$	0.001	0.02
2D CF	–	$\nu = 0.001, U_{mean} = 1m/s$	$1,001 \times 3 \times [3,000, 5,000]$	0.01	–
3D GS RD	Eq. S30	$D_u = 0.2, D_v = 0.1, \alpha = 0.025, \beta = 0.055$	$3,001 \times 2 \times 48^3$	0.25	2
2D BS	–	–	–	–	–

C.1.4 2D Hydrological Black Sea Dataset. Despite satisfactory performance, the CiGNN model is only tested on simulated datasets for systems governed by well-posed PDEs in the previous examples. However, in real-world problems, the field observation data often contains vast uncertainties induced by measurement noise, variant boundary and source conditions, etc., posing a grand challenge for data-driven modeling of complex spatiotemporal dynamics. For example, predicting precipitation in a coastal area can be substantially affected by unforeseeable extreme weather events. In light of the practical application of CiGNN, we have intentionally considered a real-world problem in the field of oceanography, namely, forecasting the hydrological dynamics of the Black Sea.

The Black Sea dataset consists of monthly and daily ocean fields of the BS basin, e.g., the daily averaged water flow velocities $u(x, y, t)$ and $v(x, y, t)$ and sea surface temperature $T(x, y, t)$, recorded from June 1, 1993 to June 31, 2021, with a horizontal resolution of $1/27^\circ \times 1/36^\circ$ and 31 levels of sea elevation¹. It is noted that the multi-year field observations located in an irregular domain encompass an intrinsic nature, e.g., low spatial and temporal resolution, limited long-term data sequence, inherent noise, data gaps, and unknown environmental influences such as immeasurable effects of climate change, among others, which would result in critical challenges in establishing a robust learning model for accurate forecasting. Nevertheless, considering the periodic patterns of the hydrological time series, we encode the cyclical timestamp into our CiGNN model to capture effectively the variations in specific portions of the dataset.

C.2 Dataset Generation

C.2.1 2D Burgers Equation. In our work, we consider the Burgers equation in a 2D setting, which is given by

$$\frac{\partial u(x, y, t \geq 0)}{\partial t} = \nu \nabla^2 u - u \frac{\partial u}{\partial x} - v \frac{\partial u}{\partial y}, \quad (\text{S28a})$$

$$\frac{\partial v(x, y, t \geq 0)}{\partial t} = \nu \nabla^2 v - u \frac{\partial v}{\partial x} - v \frac{\partial v}{\partial y}, \quad (\text{S28b})$$

$$u(x, y, t = 0) = u_0(x, y), \quad (\text{S28c})$$

$$v(x, y, t = 0) = v_0(x, y). \quad (\text{S28d})$$

Here $\nu > 0$ represents the viscous property of the fluid, and $u(x, y, t)$ and $v(x, y, t)$ denote the velocity components at the indicated spatial and temporal coordinates. Specifically, we leverage periodic boundary conditions to generate the simulation data within a spatial domain of $\Omega = (0, 1)^2$ and a time duration of $t \in [0, 1]$. The viscous coefficient ν is set to 0.01. Additionally, the initial conditions

$u_0(x, y)$ and $v_0(x, y)$ for each component are generated with:

$$\tilde{u}_0(x, y) = \sum_{a_i=0}^{n_a} \sum_{b_j=0}^{n_b} \lambda_u \cos(\iota) + \gamma_v \sin(\iota), \quad (\text{S29a})$$

$$u_0(x, y) = \frac{1}{3} \times \left(2 \times \frac{\tilde{u}_0(x, y)}{\max \tilde{u}_0(x, y)} + c_u \right), \quad (\text{S29b})$$

$$\tilde{v}_0(x, y) = \sum_{a_i=0}^{n_a} \sum_{b_j=0}^{n_b} \lambda_v \cos(\iota) + \gamma_u \sin(\iota), \quad (\text{S29c})$$

$$v_0(x, y) = \frac{1}{3} \times \left(2 \times \frac{\tilde{v}_0(x, y)}{\max \tilde{v}_0(x, y)} + c_v \right), \quad (\text{S29d})$$

$$\iota = 2\pi \left((a_i - \frac{n_a}{2})x + (b_j - \frac{n_b}{2})y \right), \quad (\text{S29e})$$

where $N = 10, \delta t = 0.001, \delta x = \delta y = 1/50, \lambda_u, \gamma_u, \lambda_v, \gamma_v \sim \mathcal{N}(0, 1)$, and $c_u, c_v \sim \mathcal{N}(-1, 1)$. The ground-truth data is calculated using a 4th-order Runge–Kutta time integration method [51].

C.2.2 3D GS RD Equation. The 3D GS RD equation is expressed by:

$$\frac{\partial u(x, y, z, t \geq 0)}{\partial t} = D_u \nabla^2 u - uv^2 + \alpha(1 - u), \quad (\text{S30a})$$

$$\frac{\partial v(x, y, z, t \geq 0)}{\partial t} = D_v \nabla^2 v + uv^2 - (\beta + \alpha)v, \quad (\text{S30b})$$

$$u(x, y, z, t = 0) = u_0(x, y, z), \quad (\text{S30c})$$

$$v(x, y, z, t = 0) = v_0(x, y, z). \quad (\text{S30d})$$

where $u(x, y, z, t)$ and $v(x, y, z, t)$ are the concentrations of chemical species. D_u and D_v are the corresponding diffusion coefficients for u and v , respectively. β is the conversion rate, α is the in-flow rate of u from the outside, and $(\alpha + \beta)$ is the removal rate of v from the reaction field.

The simulation datasets are obtained by solving the following initial-boundary value problem on $\Omega = [0, 96]^3$ with periodic boundary conditions. Moreover, we define $D_u = 0.2, D_v = 0.1, \alpha = 0.025, \beta = 0.055, \delta t = 0.25, \delta x = 2$. The initial conditions $u_0(x, y, z)$ and $v_0(x, y, z)$ for each component are generated as follows:

$$u_0(x, y, z) = (1 - rt) \times 1 + rt \times \lambda_u, \quad (\text{S31a})$$

$$v_0(x, y, z) = 0 + rt \times \lambda_v, \quad (\text{S31b})$$

where $rt = 0.1$ and $\lambda_u, \lambda_v \sim \mathcal{N}(0, 1)$. The ground-truth data is also generated by using the 4th-order Runge–Kutta time integration method.

C.2.3 2D CF Dataset. The CF dataset simulates the temporal evolution of incompressible flow past a long cylinder. It poses challenges to dynamics prediction due to the occurrence of periodic flow patterns. In this paper, we simulate CF datasets with various

¹https://data.marine.copernicus.eu/product/BLKSEA_MULTYEAR_PHY_007_004/description

positions of the cylinder and different sizes of the diameter of cylinders using the COMSOL software ². We define the spatial domain as $x \in [0, 1.2] [m]$ and $y \in [0, 0.41] [m]$ and the time duration as $t \in [0, 10] [s]$. In addition, we generate CF examples with the no-slip boundary condition.

Furthermore, we fix the median initial velocity $U_{mean} = 1 [m/s]$ and viscosity $\nu = 10^{-3} [Pa \cdot s]$, but modify the radius sizes r and the positions (c_x, c_y) of cylinders. To be more specific, we sample these two parameters uniformly where $r \in [0.04, 0.081]$, $C \in [0.1, 0.31] \times [0.1, 0.31]$ (unit: [m]). The Reynolds numbers Re are within [800, 1600]. Figure S1 shows the flow pattern around the cylinder in a free flow.

C.2.4 2D Real-world Black Sea Dataset. The Black Sea (BS) dataset is obtained using the Nucleus for European Modeling of the Ocean (NEMO) general circulation ocean model within the Black Sea domain. The NEMO model is driven by atmospheric surface fluxes computed through bulk formulation, utilizing ECMWF ERA5 [26] atmospheric fields with a spatial resolution of 0.25° and a temporal resolution of 1 hour. Additionally, the NEMO model is online coupled to the OceanVar assimilation scheme [15], allowing for the assimilation of sea level anomaly along-track observations from Copernicus Marine Environment Monitoring Service (CMEMS) ⁴ datasets. In our paper, we preprocess the spatial information by uniformly sampling 1,000 points from the total computational domain including over 40,000 real measurement points for model learning and prediction. Furthermore, we divide the data into annual units and resample the dataset with one snapshot per day to enable effective learning of periodic information in time series data. The training dataset spans from June 1, 1993, to December 31, 2017, the validation dataset covers January 1, 2018, to December 31, 2020, and the test dataset comprises data from January 1, 2021, to June 31, 2021.

C.3 Baseline Description

C.3.1 FNO. FNO is a well-recognized neural operator architecture for scientific modeling, which holds the capability to approximate any continuous operator [35]. This framework is primarily composed of stacked fourier layers, where each layer comprises two components. The first component performs a series of operations, including fourier transformation, linear transformation, and inverse fourier transformation on the input. The second component incorporates a linear transformation. Subsequently, the outputs from these two components are combined through summation and passed through an activation function to produce the final output.

C.3.2 MGN. MGN [42] introduces a “Encoder-Processor-Decoder” framework for training mesh-based simulations with graph neural networks. This framework enables the network to convey messages on a mesh graph during forward simulations. Here, the encoder captures node-specific physical information, the processor facilitates message passing across the graph, and the decoder generates prediction results. The efficacy of MGN has been demonstrated across diverse physical systems, such as solid deformation, cloth dynamics, and fluid behavior.

²<https://cn.comsol.com/model/flow-past-a-cylinder-97>

³<https://doi.org/10.5281/zenodo.1464816>

⁴<https://marine.copernicus.eu/>

C.3.3 MP-PDE. MP-PDE [8] serves as one of the state-of-the-art (SOTA) neural PDE solvers. It introduces two techniques (i.e., the pushforward technique and the temporal bundling technique) to address the instability issue arising from error accumulation in multiple-step predictions within autoregressive models. Specifically, the pushforward technique involves backpropagating solely through the last step after unrolling multiple steps, augmented by introducing adversarial perturbations to enhance model stability. The temporal bundling technique, on the other hand, is designed for the simultaneous prediction of multiple future steps. It effectively reduces solver call’s frequency and thus alleviates distribution drift and mitigates error accumulation. For a fair comparison, we omit the temporal bundling technique from the experiment, while maintaining all other settings consistent with the original method.

C.3.4 DeepONet. DeepONet [38] is another popular neural operator-based PDE solver. It comprises two distinct sub-networks: the branch network and the trunk network. They are responsible for encoding the input function and the value of the output function at a specific position, respectively. DeepONet significantly minimizes generalization errors and efficiently learns operators from the relatively small dataset.

D Experimental Setup

D.1 Treatment of Boundary Condition

We consider hard encoding of BCs to facilitate the network optimization and improve the solution accuracy. For example, the periodic padding technique has demonstrated effective to improve the model’s performance [48]. The specific implementations are: (1) labelling the nodes with different types to augment the input features and distinguish the boundary nodes; (2) padding on the boundary nodes with specified values when computing training loss. In particular, we consider two types of BCs, namely, periodic and Dirichlet. For the system with periodic BCs, we augment the graph by adding a set of ghost nodes and conduct periodic padding based on the predicted boundary node features [48]. When the Dirichlet BCs are known, we directly pad the boundary node features with the ground truth boundary values. Note that there is no specific treatment of BCs in the original GNN baseline models, such as MeshGraphNet [42] and MP-PDE [8]. To be fair, this method of BC encoding is used as a plug-in for all relevant models.

D.2 Data Normalization

We consider two aspects of the normalization in this work, namely, data normalization and parameter normalization. Instead of normalizing the input and target labels to be zero-mean and unit-variance, we learn on-the-fly the mean value and standard variance value, which have demonstrated to improve the convergence speed in the training stage. With respect to the parameter normalization, we employ the LayerNorm function [41] in the CiGNN model.

E Experimental Results

E.1 Hyperparameter Tests

The proposed model contains several hyperparameters (e.g., the standard deviation of Gaussian noise and the mask ratio) which

Table S4: Results of CiGNN and other baseline models under diverse Gaussian noises. The abbreviation “Std.” represents the standard deviation. The relevant parameters are set as follows: batch size of 10, rollout step of 1 during training, 4 SymMPNN layers, 1 mesh layer, and 1,000 epochs.

Dataset	Std. of Noise (σ)	FNO	MGN	MP-PDE	CiGNN (Ours)
2D Burgers	0	1.7089×10^{-1}	1.1953×10^{-1}	9.2760×10^{-2}	7.4002×10^{-2}
	1×10^{-4}	1.6544×10^{-1}	9.8201×10^{-2}	8.1960×10^{-2}	6.9040×10^{-2}
	1×10^{-3}	1.7066×10^{-1}	1.3491×10^{-1}	8.8580×10^{-2}	7.3760×10^{-2}
	1×10^{-2}	1.7107×10^{-1}	1.2661×10^{-1}	9.7470×10^{-2}	7.5030×10^{-2}
	1×10^{-1}	2.2164×10^{-1}	3.0238×10^{-1}	2.4177×10^{-1}	4.7619×10^{-1}
	1	3.0831×10^{-1}	3.4646×10^{-1}	3.1215×10^{-1}	3.7220×10^{-1}

Table S5: Results of CiGNN with various activation functions on four datasets. The relevant parameters are set as follows: 4 SymMPNN layers, 1 mesh layer, 1 rollout step in the training stage, and 1,000 epochs

Model	Activation Function	2D Burgers	2D CF	3D GS RD	2D BS
CiGNN (Ours)	ReLU	7.7310×10^{-2}	9.5346×10^{-1}	8.6100×10^{-2}	7.9486×10^{-1}
	ELU	7.4026×10^{-2}	9.6696×10^{-1}	1.2320×10^{-1}	7.9322×10^{-1}
	GELU	6.9040×10^{-2}	9.4314×10^{-1}	6.1142×10^{-2}	7.9282×10^{-1}
	Swish	7.6870×10^{-2}	9.6265×10^{-1}	8.1300×10^{-2}	7.9904×10^{-1}

Table S6: Results of CiGNN and other baseline models under different rollout steps. The relevant parameters are as follows: 4 SymMPNN layers, 1 mesh layer, and 1,000 epochs.

Dataset	No. of Rollout Step	FNO	MGN	MP-PDE	CiGNN (Ours)
2D Burgers	1	1.6544×10^{-1}	9.8201×10^{-2}	8.1960×10^{-2}	6.9040×10^{-2}
	2	1.6393×10^{-1}	9.8660×10^{-2}	8.1804×10^{-2}	6.0010×10^{-2}
	5	1.5432×10^{-1}	8.1890×10^{-2}	6.8288×10^{-2}	4.4463×10^{-2}
	10	1.4335×10^{-1}	6.1840×10^{-2}	5.5547×10^{-2}	9.1300×10^{-3}

Table S7: Results of CiGNN on four datasets about the number of mask ratio. The relevant parameters are set as follows: 4 SymMPNN layers, 2 mesh layers, 1 rollout step and 1,000 epochs.

Model	No. of Mask Ratio	2D Burgers	2D CF	3D GS RD	2D BS
CiGNN (Ours)	0%	6.9040×10^{-2}	9.4314×10^{-1}	6.1142×10^{-2}	7.9282×10^{-1}
	30%	7.1350×10^{-2}	9.4556×10^{-1}	6.3600×10^{-2}	7.9322×10^{-1}
	60%	6.5840×10^{-2}	9.4418×10^{-1}	6.8900×10^{-2}	8.2190×10^{-1}
	90%	6.4780×10^{-2}	9.4327×10^{-1}	4.5912×10^{-2}	7.9185×10^{-1}

Table S8: Results of CiGNN on four datasets about the number of mesh layers. The relevant parameters are set as follows: 4 SymMPNN layers, and 1,000 epochs. Here, the symbol “-” represents the phenomenon that there are not enough nodes to form a new mesh.

Model	No. of Mesh Layer	2D Burgers	2D CF	3D GS RD	2D BS
CiGNN (Delaunay)	1	6.9040×10^{-2}	9.4314×10^{-1}	6.1142×10^{-2}	7.9282×10^{-1}
	2	6.4780×10^{-2}	9.43271×10^{-1}	4.5912×10^{-2}	7.9185×10^{-1}
	3	6.4610×10^{-2}	9.43298×10^{-1}	4.5803×10^{-2}	7.9101×10^{-1}
	4	-	9.43275×10^{-1}	9.46512×10^{-2}	-

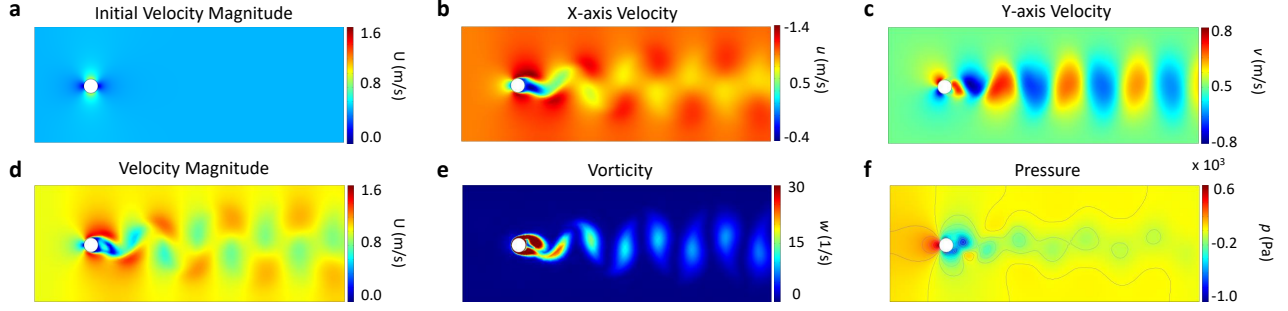


Figure S1: The snapshots of 2D unsteady incompressible CF dataset. a, the initial velocity magnitude U . b–c, the velocity components u and v at $t = 5$ s. d, the velocity magnitude U at $t = 5$ s. e, the vorticity w at $t = 5$ s. f, the pressure p at $t = 5$ s.

Table S9: Summary of each model’s performance in terms of prediction error, e.g., aggregated root mean square error (RMSE) between the predicted and ground truth test data. Here, “–” denotes the model is unable or unsuitable to learn the dynamics (e.g., inapplicable to handle irregular mesh). “Multiple*” means that no gradient is backward propagated except for the last step. The bold values and underlined values represent the optimal and sub-optimal results on various datasets.

Model	Rollout Step	2D Burgers ($\Delta t = 0.001s$)	3D GS RD ($\Delta t = 0.001s$)	2D CF ($\Delta t = 0.01s$)	2D BS ($\Delta t = 1day$)
DeepONet	Pointwise	3.7752×10^{-1}	1.3954×10^1	9.1095×10^{-1}	2.8696×10^0
FNO	One	2.2132×10^{-2}	1.4958×10^{-1}	–	–
	Multiple	1.6005×10^{-2}	1.5184×10^{-1}	–	–
MGN	One	1.7820×10^{-1}	9.8030×10^{-3}	9.3177×10^{-1}	9.9725×10^{-1}
	Multiple	1.8955×10^{-2}	1.0350×10^{-2}	<u>1.5790×10^{-1}</u>	<u>6.9512×10^{-1}</u>
MP-PDE	One	1.4210×10^{-1}	1.0190×10^{-2}	9.3982×10^{-1}	9.9533×10^{-1}
	Multiple*	1.6280×10^{-2}	1.0186×10^{-2}	2.4511×10^{-1}	9.0051×10^{-1}
	Multiple	<u>1.5551×10^{-2}</u>	1.0843×10^{-2}	1.6412×10^{-1}	6.9621×10^{-1}
CiGNN	One	4.7870×10^{-2}	<u>9.4229×10^{-3}</u>	8.2013×10^{-1}	9.2701×10^{-1}
	Multiple	4.2916×10^{-3}	8.3840×10^{-3}	1.2561×10^{-1}	6.5503×10^{-1}

Table S10: Summary of performance of CiGNN and its variants. CiGNN[–] and CiGNN* are two variants of CiGNN, where in the SymMPNN block only the asymmetric information passing is considered.

Model	Rollout Step	2D Burgers ($\Delta t = 0.001s$)	3D GS RD ($\Delta t = 0.001s$)	2D CF ($\Delta t = 0.01s$)	2D BS ($\Delta t = 1day$)
CiGNN	One	4.7870×10^{-2}	9.4229×10^{-3}	8.2013×10^{-1}	9.2701×10^{-1}
	Multiple	4.2916×10^{-3}	8.3840×10^{-3}	1.2561×10^{-1}	6.5503×10^{-1}
CiGNN [–]	One	5.0001×10^{-2}	1.1274×10^{-2}	8.2866×10^{-1}	9.0891×10^{-1}
	Multiple	5.2239×10^{-3}	1.0675×10^{-2}	1.3678×10^{-1}	6.1735×10^{-1}
CiGNN*	One	5.6548×10^{-2}	9.7794×10^{-3}	8.2520×10^{-1}	9.0788×10^{-1}
	Multiple	5.6090×10^{-3}	9.7826×10^{-3}	1.3302×10^{-1}	6.1515×10^{-1}

affect the performance of the trained model. In this part, we investigate the sensitivity of these hyperparameters w.r.t. model performance. Throughout these experiments, we maintain the batch size consistent with the settings used in the other baseline models. The raw data consists of different low-resolution data, e.g., the resolution of Burgers equation is $[50 \times 50]$ and GS RD equation $[24 \times 24 \times 24]$. Except for the BS dataset, which comprises 365 time steps, all other datasets consist of 1,000 time steps.

The quantities of the training/validation/test datasets in the hyperparameter test are given as follows: 10/5/5 (Burgers), 5/3/3 (GS RD), 50/5/5 (CF) and 10/5/1 (BS). Note that given the underperformance of DeepONet under conditions of fewer parameters and limited training data, we have excluded its related experiments from certain tests.

E.1.1 Stability and training noise. In the stage of training, we adopt a data augmentation strategy by adding the Gaussian noise $\epsilon \in \mathcal{N}(0, \sigma)$ to the input variables. Unlike the “denoising” scheme,

we utilize this method to learn the shifting from the input distribution to its corresponding output distribution. The existing research [42, 53] has shown that adding Gaussian noise to the inputs during training facilitates training stability and alleviates error accumulation. As depicted in Table S4, various Gaussian noises ϵ exhibit distinct effects on model performance. We empirically observe that, across all models, the optimal performance is achieved when injecting noise with a standard deviation $\sigma = 1 \times 10^{-4}$. Conversely, introducing noise at other levels, such as $\sigma = 1 \times 10^{-1}$, proves to be detrimental. As mentioned earlier, the substantial offset of nodes within the graph structure leads to a notable increase in solution errors.

E.1.2 Activation function. In this part, we conduct a test on activation functions (e.g., Rectified Linear Unit (ReLU) [1], Exponential Linear Unit (ELU) [13], Gaussian Error Linear Unit (GELU) [24] and Swish [47]). Note that we select $\sigma = 1 \times 10^{-4}$ as the standard deviation of the noise, based on the results in Table S4. As shown in Table S5, different activation functions yield varied performances across diverse datasets. This emphasizes the necessity to avoid a one-size-fits-all approach, especially when applying the same activation function to different datasets. The experimental results reveal comparable performance among all activation functions on the 2D BS dataset. Moreover, GELU exhibits superior performance on all datasets. Thus, we consider it as a general activation function setup for the majority of datasets in this study.

E.1.3 Effect of rollout steps. Regarding the number of rollout steps, we observe that the multi-step prediction approach employed in traditional numerical methods can be seamlessly integrated into neural networks during the training stage. This coupling scheme can effectively alleviate the issue of error accumulation in long-sequence predictions. As depicted in Table S6, training with long-horizon snapshots manifests improved performance while short-range training shows poor convergence. Therefore, the rollout steps play a critical role in learning spatiotemporal dynamics, particularly the complex PDE systems. A larger number of rollout steps facilitates the learning capability of models for spatiotemporal dynamics as well as long-horizon forecasting.

E.2 Parametric Study on Multiscale Learning

As shown in Table 2, implementing a multi-scale approach shows promise in augmenting model performance and mitigating errors. However, we also find that an excessive number of scales may result in information loss, as indicated by our following experiments. Multi-scale modeling on graphs shares fundamental principles with its counterpart on Euclidean structures. Given the distinctive characteristics of graph structures, we introduce a specialized multi-scale method designed for scaling up and down. This method enhances the efficacy of GNNs in multi-scale modeling. Furthermore, the multi-scale approach facilitates performance improvement without a significant increase in GPU consumption. In our experiments, we fix the number of mini-scale latent dimensions at 128 and employ the Delaunay triangulation algorithm [44] for mesh generation. We train the network using the Adam optimizer [31] with 1000 epochs until convergence. The initial learning rate is set to 0.0001 and is decreased by a factor of 0.8 every 100 iterations. For the initialization of network parameters (e.g., weights and biases), we employ Xavier initialization [18].

E.2.1 Effect of mask ratio. We focus on evaluating long-range dependencies within a single-scale problem. Our goal is to understand the impact of long-range dependencies on model performance both theoretically and empirically and quantify their effects. In this experiment, a mask ratio of 0 and 1 corresponds to identical conditions for two sets of experimental results. When the mask ratio is 0, it signifies that the reconstructed second-layer mesh undergoes no masking operations, indicating complete alignment with the topological structure of the first-layer mesh. Conversely, a mask ratio of 1 implies that the second-layer mesh to be reconstructed is entirely blocked, resulting in the model utilizing only the first-layer mesh. We select a representative case for the numerical experiments, and a similar rationale applies to other systems. As shown in Table S7, our results indicate that, during the masking process, preserving excessive edge information does not necessarily yield better outcomes as expected. The experimental results suggest that a limited amount of global edge information proves to be more effective.

E.2.2 Effect of mesh layers. Based on the results presented in Table S7, we have selected the specific parameters that produce the most significant performance improvement for each model. Specifically, we choose a mask ratio of 0.9 in this paper. As illustrated in Table S8, we observe that employing more mesh layers generally leads to relatively better performance, with exceptions such as the CF dataset. This discrepancy can be attributed to variations in node positions between the training and test datasets, which results in distinct computed graphs. Hence, we avoid increasing the number of mesh layers in the experiments involving the CF dataset. It is noteworthy that each graph of the Burgers equation comprises only 2,500 points, so a mask ratio of 0.9 allows for up to 2 rounds of mask operations. As the third layer consists of only 2 nodes, it is insufficient to form a complete mesh cell. A similar situation exists for the BS dataset, as each graph contains only 1,000 nodes. Considering the possibility of isolated points, we limit the maximum mesh layer to 3 in our work. Our experimental results show that the model can reduce errors when the number of local edges increases. In discrete spatial domains, additional points contribute to a more continuous function representation within the integral domain.

E.3 Ablation Study on Temporal Strategies

We hypothesize that the message-passing process of the feedforward SymMPNN layers can be viewed as the temporal propagation of dynamics of a multi-degree-of-freedom (MDOF) system, e.g., the channel features can be regarded as the MDOF state. In that case, the output latent graph features of any two adjacent SymMPNN layers should present a clear correlation. We use the Burgers dataset to test this hypothesis based on a CiGNN model with 4 SymMPNN layers. The resemblance of these feature patterns supports the aforementioned hypothesis. Hence, incorporating a temporal integration scheme to sequentially march the latent features of the feedforward SymMPNN layers has the potential to improve the model's performance for long-range temporal prediction. To this end, we considered four different temporal integration strategies in combination with two depths of CiGNN models (e.g., 4 and 16 SymMPNN layers) as listed in Table 3. It is evident that a 4-layer

CiGNN model with the simplest 1D convolution filter-based strategy (denoted by C3, with minimal parameter overhead) achieves the best performance, surpassing other strategies including the 2D convolution filtering, TCN and LSTM. However, a deeper model (e.g., 16 layers) may lead to the over-smoothness issue. The results

demonstrate that the proposed temporal integration strategy plays a key role in CiGNN to improve the model's long-term rollout prediction accuracy especially when the prediction time step remains large.

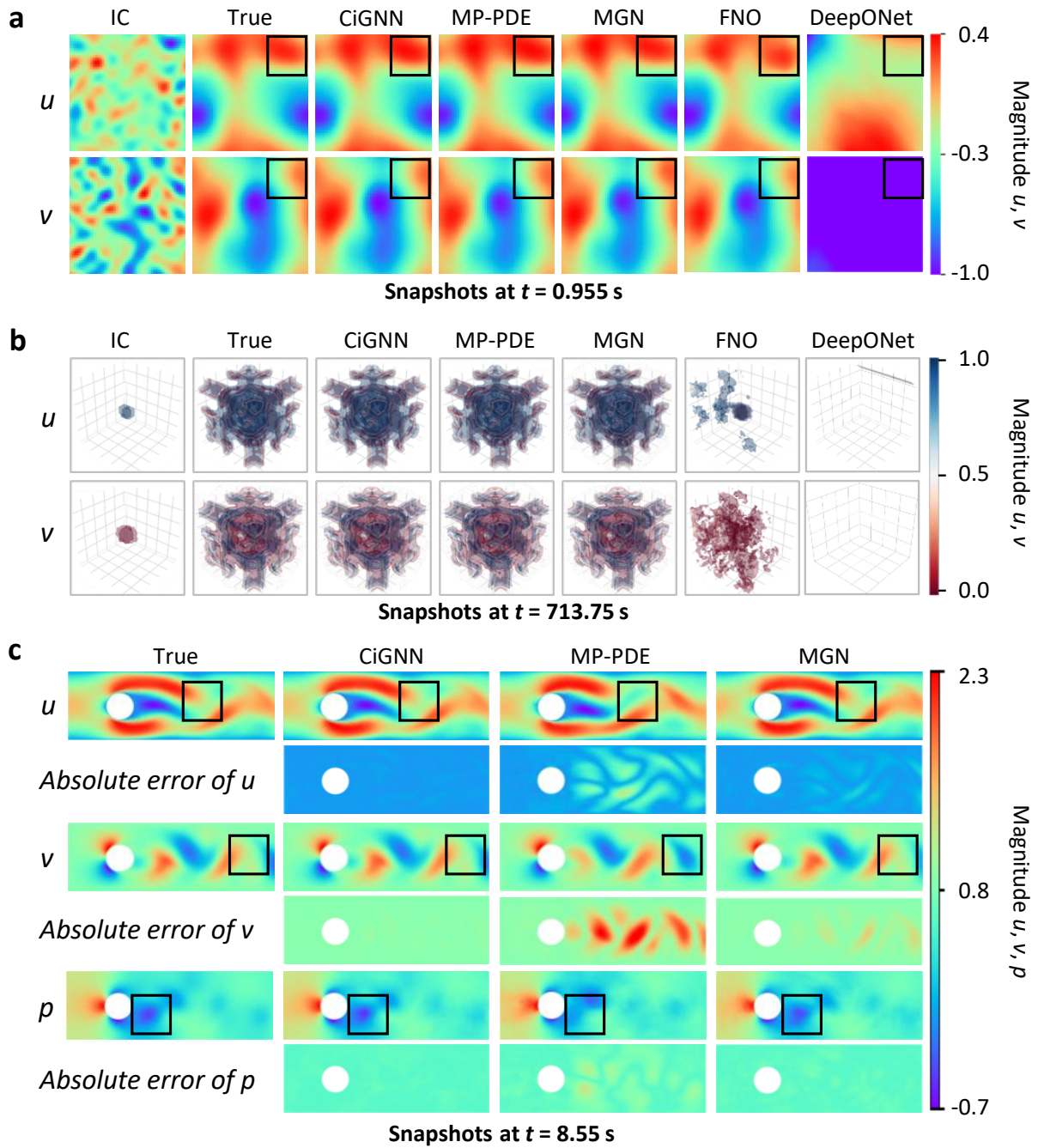


Figure S2: The system state snapshots predicted by CiGNN and other baseline models. a, the snapshots of 2D viscous Burgers equation at $t= 0.955$ s. b, the snapshots of 3D Gray-Scott equation at $t= 713.75$ s. c, the snapshots of 2D incompressible flow past a cylinder at $t= 8.55$ s. The coordinate and radius for this case is (0.30 m, 0.20 m, 0.08 m).

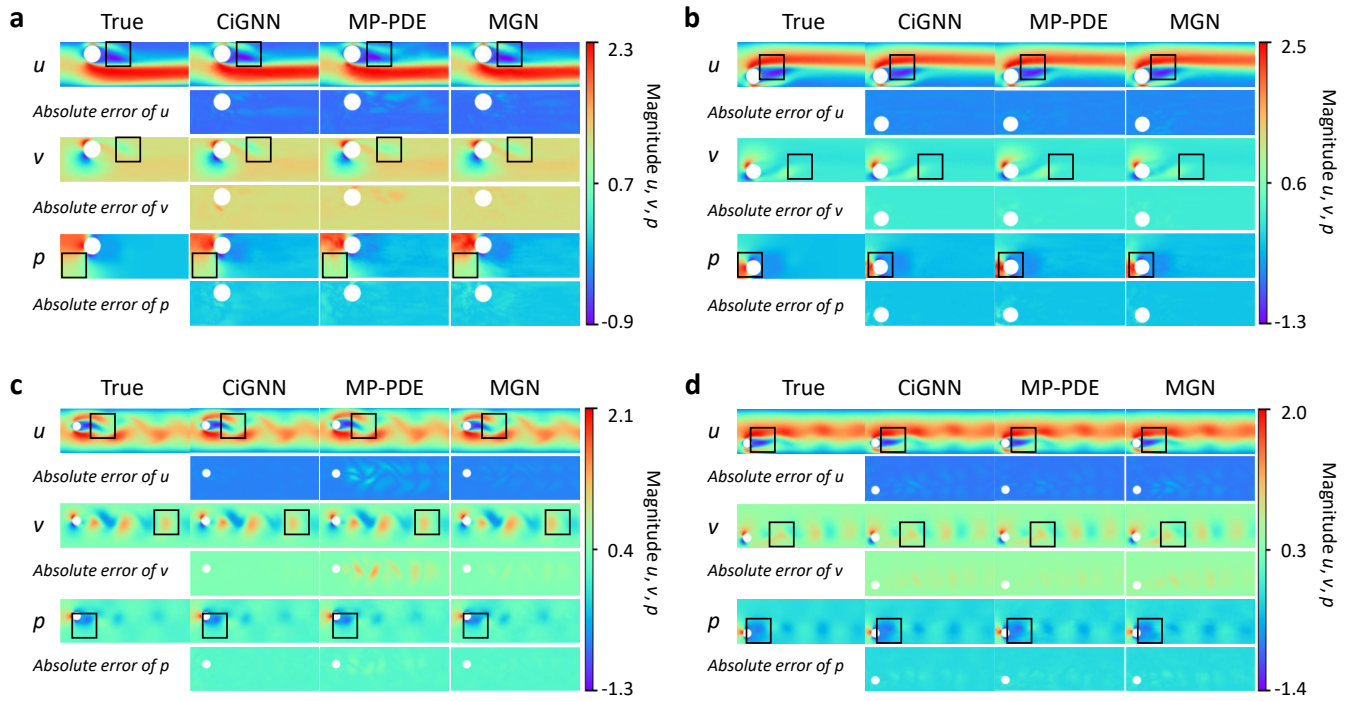


Figure S3: The generalization test snapshots of 2D unsteady incompressible CF dataset at $t = 8.55$ s. The coordinates and radius for Figures a to d are (0.30 m, 0.30 m, 0.08 m), (0.15 m, 0.10 m, 0.07 m), (0.15 m, 0.25 m, 0.04 m), and (0.10 m, 0.10 m, 0.04 m). The test datasets are employed to evaluate the generalization ability of the trained models over the change of BCs due to different positions of the cylinder.

Table S11: Range of training hyperparameters for DeepONet

Dataset	Branch Layers	Trunk Layers	Learning rate	Weight decay	Hidden dimension	Batch size	Rollout Step
2D Burgers	3	1	5×10^{-4}	1×10^{-5}	512	10	1
2D CF	1	3	5×10^{-4}	1×10^{-5}	512	1	1
3D GS RD	3	1	5×10^{-4}	1×10^{-5}	512	5	1
2D BS	3	2	5×10^{-4}	1×10^{-5}	512	10	1

Table S12: Range of training hyperparameters for FNO

Dataset	No. of Layers	Std. of Noise	Learning rate	Weight decay	Hidden dimension	Modes	Batch size	Rollout Step
2D Burgers	4	1×10^{-4}	1×10^{-4}	1×10^{-8}	32	8	10	10
3D GS RD	4	1×10^{-2}	1×10^{-4}	1×10^{-8}	16	5	10	10

Table S13: Range of training hyperparameters for MGN, MP-PDE, CiGNN and its two variants. The number of latent layers in Processor block is 4 and the hidden dimension is 128.

Model	Dataset	No. of Layers	Std. of Noise	Learning rate	Weight decay	Hidden dimension	Mask Ratio	Batch size	Rollout Step
MGN	2D Burgers	4	1×10^{-4}	1×10^{-4}	1×10^{-4}	128	–	10	10
	2D CF	4	1×10^{-2}	1×10^{-4}	1×10^{-4}	128	–	10	10
	3D GS RD	4	1×10^{-2}	1×10^{-4}	1×10^{-8}	128	–	5	2
	2D BS	4	1×10^{-2}	1×10^{-4}	1×10^{-4}	128	–	30	20
MP-PDE	2D Burgers	4	1×10^{-4}	1×10^{-4}	1×10^{-4}	128	–	10	10
	2D CF	4	1×10^{-2}	1×10^{-4}	1×10^{-4}	128	–	10	10
	3D GS RD	4	1×10^{-2}	1×10^{-4}	1×10^{-8}	128	–	5	2
	2D BS	4	1×10^{-2}	1×10^{-4}	1×10^{-4}	128	–	30	20
CiGNN	2D Burgers	4	1×10^{-4}	1×10^{-4}	1×10^{-4}	128	0.9	10	10
	2D CF	4	1×10^{-2}	1×10^{-4}	1×10^{-4}	128	0.9	10	10
	3D GS RD	4	1×10^{-2}	1×10^{-4}	1×10^{-8}	128	0.9	5	2
	2D BS	4	1×10^{-2}	1×10^{-4}	1×10^{-4}	128	0.9	30	20
CiGNN ⁻	2D Burgers	4	1×10^{-2}	1×10^{-4}	1×10^{-4}	128	0.9	10	10
	2D CF	4	1×10^{-2}	1×10^{-4}	1×10^{-4}	128	0.9	10	10
	3D GS RD	4	1×10^{-2}	1×10^{-4}	1×10^{-8}	128	0.9	5	2
	2D BS	4	1×10^{-2}	1×10^{-4}	1×10^{-4}	128	0.9	30	20
CiGNN [*]	2D Burgers	4	1×10^{-2}	1×10^{-4}	1×10^{-4}	128	0.9	10	10
	2D CF	4	1×10^{-2}	1×10^{-4}	1×10^{-4}	128	0.9	10	10
	3D GS RD	4	1×10^{-2}	1×10^{-4}	1×10^{-8}	128	0.9	5	2
	2D BS	4	1×10^{-2}	1×10^{-4}	1×10^{-4}	128	0.9	30	20